Astron. Astrophys. 288, 860–882 (1994)

ASTRONOMY AND ASTROPHYSICS

The non-LTE formation of Li I lines in cool stars

M. Carlsson[1], R.J. Rutten[23], J.H.M.J. Bruls[4], and N.G. Shchukina[5]

[1] Institute of Theoretical Astrophysics, University of Oslo, P.O. Box 1029, Blindern, N-0315 Oslo 3, Norway
[2] Sterrekundig Instituut, Postbus 80000, NL-3508 TA Utrecht, The Netherlands
[3] National Solar Observatory/Sacramento Peak, Sunspot NM 88349, USA
[4] Institute of Astronomy, ETH Zentrum, CH-8092 Zürich, Switzerland
[5] Main Astronomical Observatory, Ukrainian Academy of Sciences, Goloseevo, 252127 Kiev, Ukraine

Received 14 January 1994 / Accepted 17 March 1994

Abstract. We study the non-LTE (non local thermodynamic equilibrium) formation of Li I lines in the spectra of cool stars for a grid of radiative-equilibrium model atmospheres with variation in effective temperature, gravity, metallicity and lithium abundance. We analyze the mechanisms by which departures from LTE (local thermodynamic equilibrium) arise for Li I lines, first for the young sun (prior to its lithium depletion) and then across the cool-star grid.

There are various mechanisms which compete in their effects on emergent Li I line strengths. Their neglect produces errors in lithium abundance determinations that vary in sign as well as size, both across the stellar grid and between different Li I lines (Figs. 16–18). The errors are appreciable for all cooler stars and largest for cool lithium-rich metal-poor giants. They reverse sign between lithium-rich stars and lithium-poor stars for the $\lambda = 670.8$ nm resonance line, but not for the $\lambda = 610.4$ nm subordinate line.

The non-LTE corrections are large enough that they should be taken into account in ongoing debates on lithium synthesis and depletion. We provide convenient numerical approximations of our results (Table 1) to this purpose. We end the paper with some examples in which non-LTE corrections change the slope of published relationships.

Key words: line: formation – stars: abundances – stars: late type

1. Introduction

Lithium is a key element in studying the history of the universe, nucleosynthesis, stellar interiors and stellar evolution. It is important far in excess of its lightness, fragility and scarcity. According to standard big bang nucleosynthesis theory (Peebles 1966; Wagoner et al. 1967; Wagoner et al. 1973) most ^{7}Li was synthesized in the early universe. Measuring the primordial amount of lithium constrains big bang scenarios, the cosmic baryon density and even the neutrino family number (e.g., Truran & Cameron 1971; Yang et al. 1982; Alcock et al. 1987; Malaney & Fowler1988; Audouze & Silk 1989; Krauss & Romanelli 1990; Mathews et al. 1990; Reeves et al. 1990; Walker et al. 1991). The meteoritic lithium abundance is $n_{\rm Li}/n_{\rm H} = 2 \times 10^{-9}$ where $n_{\rm Li}/n_{\rm H}$ denotes the atomic number density ratio of ^{7}Li to hydrogen, or $A_{\rm Li} = 3.3$ where $A_{\rm Li} \equiv \lg(n_{\rm Li}/n_{\rm H}) + 12$ (Anders & Grevesse 1989); a similar value has recently been obtained for the interstellar medium (Lemoine et al. 1993). The solar lithium abundance is only $A_{\rm Li} \approx 1.1$ (e.g., Greenstein & Richardson 1951; Grevesse 1968; Engvold et al. 1970; Mueller et al. 1975; Steenbock & Holweger1984; Pavlenko 1989). The hundredfold difference originates because cool stars reduce their surface lithium through low-temperature Li(p,α)He depletion plus envelope mixing, as suggested by Greenstein & Richardson (1951) and studied in the sixties by Bodenheimer (1965), Iben (1965, 1966, 1967), Herbig (1965) and Wallerstein et al. (1965). In the classical picture laid down by these pioneers, one should regard the meteoritic lithium abundance $A_{\rm Li} = 3.3$ or the similar value measured from young stars as the primordial big-bang one.

However, this view has in the meantime been upset by a number of observations and subsequent interpretations, making the lithium "problem" a confused one. We refer the reader to its many reviewers (Boesgaard & Steigman 1985; Boesgaard 1988, 1990a, 1990b; Rebolo 1990, 1991; Spite 1990, 1991; Michaud & Charbonneau 1991) and the proceedings edited by Antona (1991), while restricting the discussion here to a summary in the form of an issue list with only key references plus recent ones.

Population II stars. Spite & Spite (1982) found to their surprise that halo dwarfs have only $A_{\rm Li} = 2.1$, with small spread between different stars. Have the halo stars all depleted their primordial $A_{\rm Li} = 3.3$ lithium content to $A_{\rm Li} = 2.1$, or have the young stars in the galactic disk all been lithium-enriched to well above a primordial value of $A_{\rm Li} = 2.1$?

Send offprint requests to: M. Carlsson

This order of ten difference in the required big bang production of lithium is the principal question in lithium studies. It hinges on the small dispersion of the halo dwarf lithium content (cf. Spite 1990, 1991; Hobbs & Thorburn 1991; Deliyannis & Pinsonneault1992; Deliyannis & Demarque 1991a,1991b; Pinsonneault et al. 1992). Deliyannis & Demarque designate the flatness of the halo dwarf lithium abundances over $T_{\rm eff}$ = 5800 – 6500 K as the "Spite plateau", taking the term plateau from Spite et al. (1984). It is not only flat in $T_{\rm eff}$, but also in metallicity [Fe/H] and in nitrogen content [N/H] (Spite & Spite 1986), and it is remarkable for its small scatter. Similar homogeneity is shown by field dwarfs of low metallicity (Rebolo et al. 1988).

These properties together underlay the belief that the halo dwarf $A_{\rm Li}$ = 2.1 lithium abundance equals or is close to the primordial big bang value, without much subsequent stellar depletion (Spite et al. 1984), and may also indicate pre-galactic conditions if the oldest stars have been accreted by the Galaxy (Cayrel 1991). However, it is also argued that the old dwarfs have reached lithium uniformity through stellar lithium depletion (Michaud et al. 1984; Proffit & Michaud1990; Vauclair 1988).

New input comes from studying the ^{6}Li/^{7}Li isotope ratio (Smith et al. 1993), from Be and B observations for halo dwarfs which show a Be excess and a B deficit over expectations (Gilmore et al. 1991; Gilmore et al. 1992; Malaney 1992; Duncan et al. 1992), from some halo dwarfs that have solar-like lithium abundance or even less (Molaro 1991; Thorburn 1992; Thorburn & Beers 1993; Spite et al. 1993), and from lithium abundances in metal-poor subgiants (Pilachowski et al. 1993). Recently, Spite & Spite (1993) have added evidence to the suggestion of Rebolo et al. (1988) that their plateau slopes, having a slight increase of $A_{\rm Li}$ for increasing effective temperature.

Old solar-type stars. The classical lithium depletion with age in main-sequence stars with $T_{\rm eff} \lesssim 6000$ K still requires detailing of the pertinent processes. The present solar lithium abundance constrains convective overshoot modeling (e.g., Schwarzschild 1957; Schatzman & Baglin 1991; Ahrens et al. 1992; Christensen-Dalsgaard et al. 1992). Mass loss is a less likely candidate (Swenson & Faulkner 1992), but momentum loss due to a stellar wind seems to work and may have affected old Population II dwarfs as well (Zahn 1992).

The star α Cen A has solar-like lithium content (Chiemelewski et al. 1992), but the well-studied old solar-like subdwarf β Hyi (Dravins et al. 1993a, b, c) has much more ($A_{\rm Li}$ = 2.4), as do old solar-type stars in NGC 188 (Hobbs & Pilachowski1988). Such stars may deepen their convection on the way to the giant stage and dredge lithium up (Dravins et al. 1993), perhaps angular momentum as well (Ambruster et al. 1992). Old stars of larger effective temperature than the sun, but cooler than the F stars discussed below, are generally much less depleted (Lambert et al. 1991).

Red giants. The survey of 644 bright giants by Brown et al. (1989) shows that most giants are depleted in lithium to values below $A_{\rm Li}$ = 1.5; only about 5% reach this value. The others are considered lithium deficient; examples are the primary of Capella (Pilachowski & Sowell 1992) and the cooler AGB (asymptotic giant branch) N stars which typically have only $A_{\rm Li} = -1$ (Denn et al. 1991).

Only a few percent of the giants are lithium rich. These include massive AGB stars (Smith & Lambert 1990) and some active giants, both single ones (Fekel & Balachandran 1993) and RS CVn binaries (Pallavicini et al. 1992; Randich et al. 1992), that are discussed below. Barium stars used to have more lithium than fit to be explained by binary mass transfer (Barbuy et al. 1992; Smith & Lambert 1986) but recently, Lambert et al. (1993) have attributed the observed overabundance to an unidentified blend in the 670.8 nm line. Finally, there are eight or so special stars that are super-rich in lithium and are also enriched in other elements. The prime example is the carbon star WZ Cas (McKellar 1940; Spitzer 1949; cf. Fig. 6 of Boesgaard 1988), which may have a lithium abundance as high as $A_{\rm Li}$ = 6.5 (Denn et al. 1991; cf. Abia et al. 1991).

The lithium-rich red giants apparently produce new lithium from inside, irrespective of what lithium they showed originally (e.g., Cameron 1955; Cameron & Fowler 1971; Scalo & Ulrich1973; Sackmann & Boothroyd 1992). They may enrich galactic lithium in general (Smith & Lambert 1989, 1990; Antona & Matteucci 1991), if sufficiently numerous (Scalo 1976).

F-star dip. The best-established lithium abundance phenomenon is the deep dip for F-stars, over nearly two orders of magnitude for $T_{\rm eff}$ = 6400 – 6800 K. It was discovered in the Hyades (Boesgaard & Tripicco 1986), may just start to develop in the Pleiades (Soderblom et al. 1993), and is also seen in other clusters (cf. Boesgaard 1991; Balachandran 1991). Various theoretical mechanisms have been proposed (e.g., Pinsonneault et al. 1990; Michaud & Richer1991; García López & Spruit 1991a, 1991b; Charbonnel & Vauclair 1992; Charbonnel et al. 1992; Dearborn et al. 1992) which all reproduce the observed dip to some extent. Schatzman (1991) argues that mixing by internal gravity waves is most likely (cf. Schatzman & Baglin 1991); this mechanism has been worked out by García López & Spruit (1991b). New information may come from the existence or absence of a similar dip for B I (Lemke et al. 1993) and O I (García López et al. 1993).

Young solar-type stars. G dwarfs tend to show $A_{\rm Li}$ = 3.0 – 3.3 when they are young, taken to be the initial Population I abundance. When do they lose their lithium? Soderblom (1991) and others compare lithium line strengths between the Pleiades (age about 70 Myr) and the Hyades (about 600 Myr) (cf. Duncan & Jones 1983; Balachandran et al. 1988; Stauffer et al. 1993; Soderblom et al. 1990, 1993a, 1993b, 1993c; Thorburn et al. 1993). The scatter is much smaller for the Hyades than for the Pleiades, indicating that lithium abundances converge with stellar age from large to small intrinsic spread. On the other hand,

the even younger α Persei cluster contains stars with anomalously low lithium abundance while data from the Ursa Major Group indicates that lithium depletion takes place both pre-main sequence and on the main sequence (Soderblom et al. 1993).

The Pleiades scatter correlates roughly with stellar rotation and with chromospheric activity as indicated by fill-in of Hα and Ca II 854.2 nm, in the sense that faster rotating stars tend to be more active and to possess more lithium (Soderblom 1991; Soderblom et al. 1993). Tidally-locked close binaries in the Hyades also seem overly lithium-rich (Thorburn et al. 1993).

Pre-main-sequence stars. T Tauri stars tend to have much lithium (Hunger 1957; Bonsack & Greenstein 1960), or even too much: Strom et al. (1989); Padgett (1990) and Basri et al. (1991) found T Tau lithium abundances well above the $A_{\rm Li} = 3.3$ meteorite value. Such superabundances may hold only for the more massive pre-main-sequence stars (Rebolo 1991), as predicted by the depletion theory of Pinsonneault et al. (1989), but are not supported by the age and mass correlations of Strom et al. (1989). They are sensitive also to spectral veiling, the presence of accretion disks, and non-LTE (non local thermodynamic equilibrium) line formation discussed below (Duncan 1991; Martin et al. 1992); Magazzu et al. (1992) obtain smaller spread from appropriate corrections and find the initial T Tau lithium content to equal the meteoritic value.

On the dwarf side, the presence of lithium may be a useful discriminator between low-mass stars and non-stellar brown dwarfs which do not reach lithium-burning temperatures (Magazzu et al. 1991; Rebolo 1991; Rebolo et al. 1992).

Correlations with activity. Duncan (1981) studied correlations between lithium line strength and chromospheric emission in Ca II H & K. Both diminish with stellar age, but in general there is no outspoken correlation between them. Giampapa (1984) suggested, from the strength of Li I 670.8 nm in sunspot umbrae where Li I is the dominant ionization stage, that Li I might be an indicator of stellar spottedness. However, rotational modulation of Li I 670.8 nm hasn't been found (Boesgaard 1990a), not even for the spotted RS CVn stars (Pallavicini et al. 1993) which sometimes, but not always, have strong Li I lines (Pallavicini et al. 1992; Randich et al. 1992, 1993) as do many single active giants (Fekel & Marschall 1991; Fekel & Balachandran 1993) with some exceptions (DeMedeiros & Lebre 1992).

Many of the lithium-rich active stars are probably post-main-sequence rather than pre-main-sequence; the questions are whether or how they have repleted depleted lithium, and whether or how that connects with chromospheric activity in evolved stars (Xue-Fu et al. 1992; Randich et al. 1993). On the other hand, for the young stars in the Pleiades the observed correlation between Li I line strength and chromospheric emission (Soderblom 1991; Soderblom et al. 1993) may derive from joint dependence on rotation-induced magnetism.

Galactic lithium production. Galactic lithium enrichment must occur if one accepts the Spite plateau stars as representative of the primordial big bang value. Sources of new lithium must then be identified that increased the galactic disk lithium content from the halo star value ($A_{\rm Li} \approx 2.1$) to the present initial Population I and meteorite value ($A_{\rm Li} \approx 3.3$). There are many candidates apart from the lithium-rich red giants mentioned above. Cosmic ray spallation is probably a minor one but it is the one most extensively discussed (e.g., Reeves et al. 1970, 1990; Meneguzzi et al. 1971; Meneguzzi & Reeves 1975; Steigman & Walker 1992; Steigman 1993; cf. Duncan et al. 1992; Olive & Schramm 1992). Other high-energy candidates include pre-main-sequence activity, novae (Antona & Matteucci 1991), supernova shocks (Dearborn et al. 1989; Brown et al. 1991), and accretion disks (Jin 1990). Stellar sources are also required to maintain the ^{7}Li/^{6}Li ratio (Reeves 1993) to the interstellar measurement of Lemoine et al. (1993). Brown (1992) discusses galactic evolution for a number of lithium sources. Murphy et al. (1990) analyzed γ-ray lines from lithium and beryllium in a solar flare and estimate a production of 10^{29} ^{7}Li nuclei per flare. Martin et al. (1992) measure the unexpectedly strong Li I 670.8 nm line from the secondary of the black hole candidate V404 Cygni, first identified (per plastic ruler) by Wallerstein (1992).

In most of these lithium debates the observational analyses depend on comparing the apparent amount of lithium in different stars. For similar stars this may be done in terms of observed line strength (e.g., Soderblom et al. 1990, 1993a) but in general, one needs to measure the atmospheric lithium abundance. In this paper we address the conversion from line strength to abundance, emphasizing departures from LTE in Li I line formation. We expand earlier Li I non-LTE analyses (Mueller et al. 1975; De la Reza et al. 1981; Steenbock & Holweger 1984; Pavlenko 1989, 1990, 1991a, 1991b; Magazzu et al. 1992) with a more comprehensive study. Our aim is not to specify non-LTE abundance corrections for specific stars, but rather to model Li I line formation across an extensive grid of stellar atmospheres, to analyze the nature of the pertinent non-LTE mechanisms, and to provide a numerical recipe for their evaluation.

Our modeling is not complete because we prefer to go for self-consistency within the constraints of classical modeling. Thus, the model atmospheres employed below do not account for chromospheres, atmospheric extensions or accretion disks. The intention is not to discriminate between the many lithium depletion and creation scenarios that are presently in debate, but rather to scrutinize the underlying measurement process. We not only estimate non-LTE corrections, but also supply experimentation and sensitivity analysis in order to understand how they arise. The study was triggered by Duncan's (1991) suggestion that non-LTE scattering may produce appreciable difference between Li I 670.8 nm and Li I 610.4 nm from BP Tau, and was inspired by non-LTE insights from solar alkali spectra.

The paper is structured as follows. The next section summarizes previous non-LTE work, in order to define which mechanisms and which modeling pitfalls may be important for Li I. Section 3 defines our method and input data, We present results in Sect. 4, first studying lithium line formation for the young sun (Sects. 4.1 and 4.2) and then for a grid of stellar atmospheres

(Sect. 4.3). The corresponding LTE to non-LTE corrections are displayed in Sect. 4.4 and given in numerical form in Sect. 4.5. We discuss our results in Sect. 5, adding various applications to published data, and we end the paper with conclusions in Sect. 6.

2. Previous non-LTE studies

This paper is a sequel to studies of non-LTE formation of alkali lines in the solar spectrum, in particular the analysis by Bruls et al. (1992). To take solar non-LTE modeling as a lead is not a new tactic. In fact, the original Li I solar non-LTE analysis by Mueller et al. (1975) has often been taken to imply that departures from LTE may be neglected in stellar lithium abundance determinations (e.g., Duncan 1981; Spite & Spite 1982). However, Li I non-LTE effects that depend on line strength may be much larger for stars with more lithium than the sun contains now ($A_{\rm Li} = 1$). It is better to use the solar K I and Na I spectra as guide for these, since these alkalis combine similar atomic structure with sufficiently high abundance ($A_{\rm K} = 5.13$ and $A_{\rm Na} = 6.31$, Anders & Grevesse 1989) to expose lithium-like non-LTE formation mechanisms more clearly (cf. Cohen 1974; Padgett 1990).

What are the non-LTE phenomena one should expect for Li I? Bruls et al. (1992) give detailed solar results for a variety of mechanisms in K I and Na I that are relevant also for lithium line formation in stars. We summarize these in the same order as they are discussed by Bruls et al. (1992).

Resonance line scattering and photon loss. The solar K I and Na I resonance lines are accurately described by the classical two-level approximation for a scattering line. Their source functions drop far below the local Planck function due to outward photon loss; they start to do so well below optical depth unity at line center because scattering propagates the loss to deep layers. Appreciable non-LTE line strengthening results. The increase is smaller for smaller abundance; for sufficiently weak lines, resonance scattering disappears when line photons are more likely used in continuum extinction processes than in line extinction. Across the lithium abundance range, Li I 670.8 nm varies from such weak-line character to resonance scattering in behavior.

Photon suction. Bruls et al. (1992) identified a process in solar K I which they termed "photon suction" and which operates also in other minority ionization stages. It results from photon losses in the resonance lines and in other lines with large transition probability at higher excitation energy. Their combined photon losses siphon a replenishment flow down from the population reservoir in the first ionization stage which resembles the collisional-radiative recombination flow in planetary nebulae. In the solar spectrum this replenishment causes the long-enigmatic emission features in the 12 μm Rydberg lines of Mg I and in infrared lines of other neutrals (Brault & Noyes 1983; Carlsson et al. 1992); for explanation see Rutten & Carlsson (1994). For resonance lines, the siphoning increases the opacity; it causes the surprisingly large populations of the K I and Na I ground states in the solar photosphere. For sufficiently large lithium abundance, it may operate in Li I as well.

Ultraviolet overionization. The classical non-LTE phenomenon affecting neutral minority stages in the solar spectrum is overionization from levels that are a few electronvolts below the continuum; the prime example is Fe I (Lites 1972; Athay & Lites 1972; cf. Rutten 1990). Such overionization arises because, even in radiative equilibrium, the angle-averaged mean intensity J_ν drops less steeply than the Planck function B_ν with height on the blue side of the solar spectrum peak. This $J_\nu - B_\nu$ radiation excess is largest for the $\lambda = 300 - 400$ nm wavelength range, in which the solar continuum originates from deep layers. Its radiation temperature exceeds the local electron temperature appreciably. However, the enormous crowding of spectral lines in the near ultraviolet, especially from iron, into a quasi-continuous "line haze" reduces the resulting continuum pumping for metal-rich stars. In addition, it is intrinsically weak for the ground states of the alkalis because these have abnormally small photo-ionization cross-sections (K I in particular).

For Li I, the threshold for photoionization from the first excited level $2p\,^2\mathrm{P}^o$ is at $\lambda = 349.8$ nm where the $J_\nu - B_\nu$ excess is largest for the solar photosphere; this channel provides most overionization in cool-star atmospheres (cf. Auman & Woodrow 1975). The size of the $J_\nu - B_\nu$ excess depends on temperature and metallicity, while its effect on the emergent line strength increases with the lithium abundance because the latter controls the sampling height.

There is a marked difference between the neutral alkalis and spectra such as Fe I. For the latter, overionization from levels at about 3–4 eV from the continuum is the dominating non-LTE effect. It reduces the opacities of all solar Fe I lines in the visible, but it does not affect their source functions because the corresponding Fe I levels are coupled more strongly by the much stronger Fe I lines in the near ultraviolet. These lines are still opaque and thermalized in the photosphere, keeping the local excitation equilibrium close to thermal. Thus, in Fe I only the photospheric ionization equilibrium departs markedly from LTE (cf. Rutten 1988). For the alkalis, however, even the resonance lines are already optically thin (or, for Na I D, effectively thin) in the upper photosphere where ultraviolet overionization occurs. Thus, for solar alkali lines non-LTE ionization and non-LTE excitation interact in controlling photospheric line formation. The same will be the case for Li I unless the lithium abundance is small.

(Infra)red overrecombination. At long wavelengths J_ν drops below B_ν, again also when radiative equilibrium holds. This reverse excess contributes to recombination in bound-free edges from high-excitation levels. It competes with the suction replenishment flow discussed above and with collisional recombination. The latter tends to dominate for long wavelength edges where the typical kinetic energy of 1 eV exceeds the threshold energy.

Bound-bound pumping. Finally, the neutral alkali spectra have a bound-bound transition from their ground state which is pumped by (ultra)violet radiation in similar fashion as the bound-free pumping discussed above. For Li I this is the $3p\ ^2P^o$—$2s\ ^2S^e$ line at $\lambda = 323.26$ nm (cf. Fig. 3). The solar K I example indicates that this pumping may increase the Li I $3p$ population appreciably, the $3s$ and $2p$ populations to smaller extent, and reduce the ground-state ($2s\ ^2S^e$) population slightly.

How well have these various processes been treated in the existing Li I line formation literature? The initial solar analysis by Mueller et al. (1975) treated the resonant scattering correctly, but sets no example for higher-abundance studies since the solar line is so weak. Müller et al. treated photoionization incorrectly by adopting $J_\nu = B_\nu$ in order to better fit the observations. Their Li I model atom was too small for modeling photon suction, overrecombination or the pumping line correctly.

Luck (1977) computed non-LTE corrections for a stellar-atmosphere grid with different effective temperatures $T_{\rm eff}$, gravities $\lg g$ and lithium abundances. He employed a better model atom, reaching up to $4d\ ^2D^e$, and treated the photoionization from the ground and first excited states in detail, noting that ultraviolet overionization from $2p$ dominates. The resulting non-LTE corrections are all positive, reaching up to 0.7 dex. Luck noted that they may be overestimated because he did not allow for the existence of the ultraviolet line haze.

De la Reza et al. (1981) used a similar Li I model atom but stipulate photoionization by ad-hoc radiation temperatures taken to represent irradiation by a hot overlying chromosphere. They modeled seven late-type dwarfs, with resulting lithium abundances up to $A_{\rm Li} = 3$. They did not specify non-LTE corrections but mention that the ratio of the 670.8 nm line source function S_l to the Planck function B_ν flips sign with effective temperature $T_{\rm eff}$.

Steenbock & Holweger (1984) modeled Li I non-LTE line formation in various types of cool stars with a slightly larger model atom, but only for small lithium abundance (left unspecified). They improved on Luck (1977) by including the ultraviolet line haze and by including, tentatively, extra thermalization thought to arise from collisions with neutral hydrogen atoms. Their non-LTE corrections are again all positive due to domination by ultraviolet overionization, and range up to 0.3 dex.

Pavlenko's cool-star studies (spectral classes K and M) constitute the most extensive Li I non-LTE modeling thus far (Pavlenko 1989, 1990, 1991a, 1991b and have led to recent application to T Tau stars by Magazzu et al. (1992). Pavlenko found larger non-LTE departures than Steenbock & Holweger (1984) and ascribed the difference to line-haze formalisms. Magazzu et al. (1992) find upward non-LTE corrections of 0.3–0.6 dex for $T_{\rm eff} < 4500$ K, smaller corrections for larger temperature, and negative corrections for $A_{\rm Li} > 3$. These were used by Martin et al. (1992) to reduce LTE-fitted lithium abundances in pre-main-sequence stars, and in a footnote to Magazzu et al. (1991) to increase the lithium abundance of UX Tau B from $A_{\rm Li} = 2.3$ to $A_{\rm Li} = 3.2$.

None of the above studies used atomic models up to the Rydberg regime, specified non-LTE corrections for other Li I lines than $\lambda = 670.8$ nm, or analyzed in detail how non-LTE processes other than ultraviolet overionization affect the results. They leave a clear need for a more extensive study with a larger stellar grid, a larger Li I model atom, addressing more Li I lines, and seeking understanding through experimentation. We supply such a study here.

3. Method and input data

The atmosphere grid contains models with the following values of effective temperature $T_{\rm eff}$ (K), surface gravity $\lg g$ (cgs units) and metallicity [Fe/H] (logarithmic departure from solar metal abundance):

$$T_{\rm eff} = [4500, 5000, 5500, 6000, 6500, 7000, 7500],$$
$$\lg g = [0.0, 2.0, 4.0, 4.5],$$
$$[{\rm Fe/H}] = [-3, -2, -1, 0].$$

The hottest model present for $\lg g = 0$ is the one with $T_{\rm eff} = 6000$ K, for $\lg g = 2$ the one with $T_{\rm eff} = 6500$ K.

The model atmospheres were computed with the Uppsala MARCS code of Gustafsson et al. (1975) with continuous absorption coefficients updated according to Mathisen (1984). These are standard plane-parallel, line-blanketed, LTE, flux-constant atmospheres. Radiative equilibrium holds in the higher layers. Convection affects the deeper layers; it is treated in the mixing length approximation setting $l/H_p = 1.5$. The line blanketing is treated in the ODF (Opacity Distribution Function) approximation.

For comparison purposes we show additional lithium results in Sect. 4.4 computed with the OS (Opacity Sampling) version of the MARCS code (Edvardsson et al. 1993), where the sampling is based on the extensive line lists compiled by Kurucz (cf. Kurucz 1990, 1991). The differences which the ODF and OS formalisms produce in the resulting atmospheric stratifications are small and therefore not shown here. However, their effect on lithium abundance determination is non-negligible, because both LTE abundance estimation and non-LTE abundance corrections are sensitive to slight changes in temperature gradient, the non-LTE corrections primarily through the dependence of the lithium ionization balance on the ultraviolet radiation fields. Examples of the latter are shown for the solar case in Fig. 8 below. The effects of ODF–OS differences on the results are discussed in Sect. 5.

A selection of atmospheres from our grid is shown in Figs. 1 and 2, respectively displaying the temperature and electron density stratifications. The solid curves are for solar metallicity, the dashed ones for metal-poor stars with [Fe/H] = −2. The metallicity affects the temperature stratification in the deepest layers for cool stars, especially dwarfs (upper-left panel), where the opacities influence the convection. The temperature gradient flattens for low metallicity in the upper layers of the warmer stars (lower panels of Fig. 1) because these become transparent for the bulk of the flux. The electron density at given optical

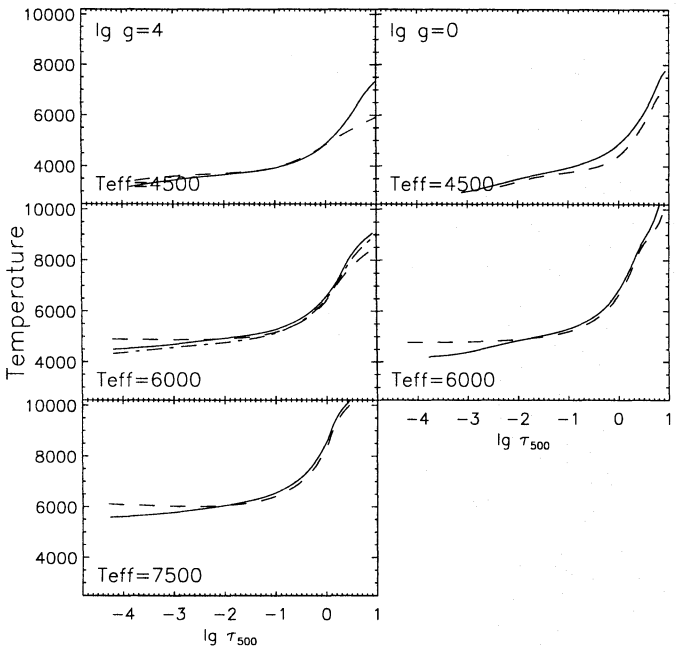

Fig. 1. Temperature in K against optical depth for a selection of flux-constant models from our grid. The effective temperature $T_{\rm eff}$ is specified per panel; the surface gravity $\lg g$ at the top of each column. (There are no models for giants with $T_{\rm eff} > 6000$ K.) Abscissae: logarithm of the continuum optical depth at $\lambda = 500$ nm. Solid: solar abundances, i.e., metallicity [Fe/H] = 0. Dashed: metal-poor stars with [Fe/H] = −2. Dot-dashed (middle-left panel): temperature stratification of the T5780 solar model atmosphere

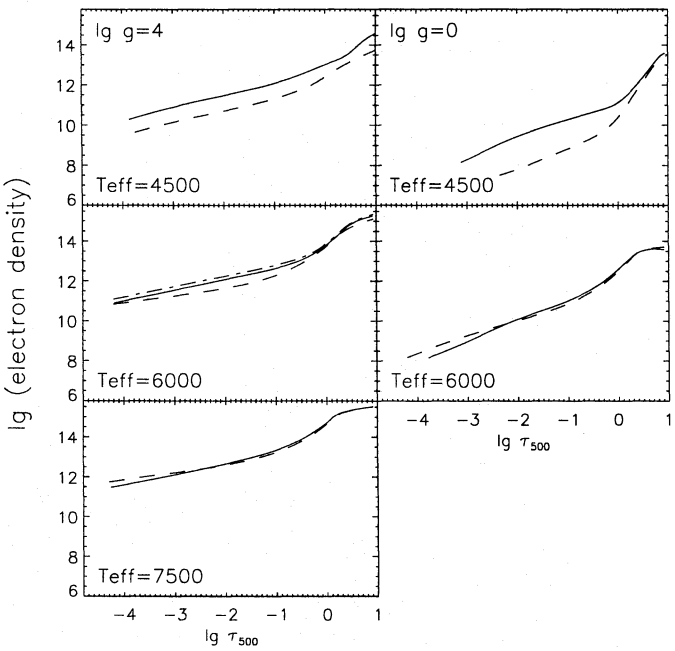

Fig. 2. Electron density in $\rm cm^{-3}$ against optical depth, for the same atmospheric models and with the same curve coding as in Fig. 1

depth goes down appreciably with metallicity in the case of cool stars, by up to two orders of magnitude (upper panels of Fig. 2).

The dot-dashed curves in the middle-left panels of Figs. 1 and 2 are for the T5780 model of the solar photosphere. This is an elaborate Uppsala model taken from Edvardsson et al. (1993). It is built on the same assumptions as our Opacity Sampling grid (cf. above) with an effective temperature of 5780 K. Its stratification is close to the ($T_{\rm eff} = 6000$, $\lg g = 4$, [Fe/H] = 0) MARCS result in the same panels.

We solve the statistical equilibrium and radiative transfer equations for all relevant levels and frequencies in Li I for each model atmosphere of the grid. We use the operator perturbation technique of Scharmer & Carlsson (1985) as coded in the program MULTI by Carlsson (1986). We employ MULTI version 2.0, in which line blanketing is taken into account in the photoionization by reading in the radiation field computed together with the atmospheric model by MARCS, as a function of height and frequency. The treatment of background opacities is improved in MULTI's version 2.0 by accounting for molecules in the number density evaluations following Gustafsson (1973), while the many-level treatment is speeded up by using the local operator of Olson et al. (1986) (cf. Puls & Herrero 1988).

The lithium model atom employed in this paper is illustrated by its Grotrian diagram in Fig. 3. It is complete up to principal quantum number $n = 9$, containing 21 levels and all transitions between them except that there is no l-splitting for $n > 6$. Our doublet "levels" are actually terms, combining the fine structure into one state with one exception; the fine structure of the 670.8 nm line is entered by assuming detailed balance between the $2p$ levels.

Level energies are from Bashkin & Stoner (1975). Oscillator strengths are from Wiese et al. (1966) for transitions with lower level up to $n = 5$, from Biémont & Grevesse (1973) for transitions with lower level $6s$, $6p$ and $6d$, and hydrogenic for the other high-n transitions.

Photoionization cross-section are from Hofsaess (1979) except for photoionization from levels $5f$-g, $6f$-h and $n > 6$ where hydrogenic cross-sections have been used. The adopted photoionization cross-sections are consistent with the values from the opacity project (Peach et al. 1988) to within 6%. In particular, the agreement for the important photoionization from $2p$ is within 1%.

All bound-bound electron collision strengths are from Park (1971), the bound-free collision strengths from Seaton as given by Allen (1976). Collisions with neutral hydrogen have not been included. There are reasons to believe that the formulae of Drawin (1968, 1969) overestimate the neutral hydrogen collisional cross-section by several orders of magnitude (see Caccin et al. 1993 for a discussion). The newer calculations by Kaulakys (1985, 1986) indicate that collisions with neutral hydrogen should be insignificant compared with electron collisions, with the possible exception of l-changing collisions between high-n levels. For the latter, electron collisions already produce Boltzmann partitioning over angular quantum number anyhow.

Radiative damping is included for all lines and has been calculated from the lifetimes of the levels. Van der Waals damping

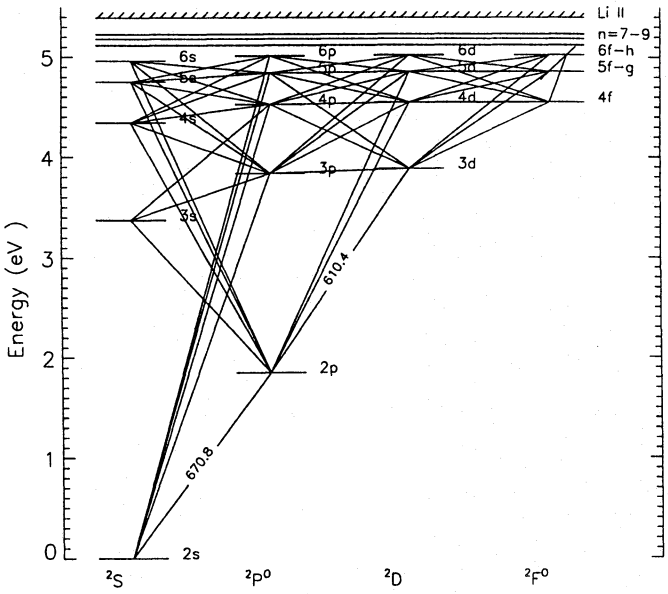

Fig. 3. Grotrian diagram for Li I. For clarity, all permitted downward transitions from $n = 7 - 9$ are omitted here but they are included in the model atom, which contains 21 levels, 70 lines and 20 bound-free transitions in total. The 670.8 nm line corresponds to the $2p$–$2s$ resonance doublet, the 610.4 nm line to the $3d$–$2p$ triplet, the 323.3 nm pumping line to $3p$–$2s$. The $2s$ bound-free edge is at $\lambda = 229.9$ nm, the $2p$ edge at 349.8 nm

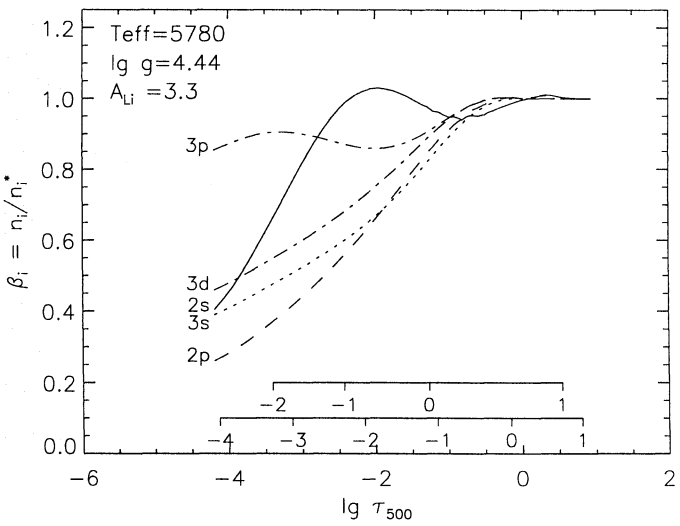

Fig. 4. Non-LTE departures for Li I in the young sun, i.e., with lithium abundance equal to the meteoritic value $A_{\rm Li} = 3.3$. Departure coefficients $\beta_i = n_i/n_i^*$ are plotted against the logarithm of the continuum optical depth at $\lambda = 500$ nm, for the lower five levels in Fig. 3. The two inset lg τ scales are respectively for the continuum optical depth at $\lambda = 670.8$ nm (lower scale) and for the total line-center optical depth at $\lambda = 670.8$ nm (upper scale). Line opacities depart from LTE by the β-value of the lower level, whereas line source function departures scale with the upper-to-lower ratio β_u/β_l. The general outward decrease is due to overionization from $2p$ and $2s$. The humps and dip in the $2s$ curve are typical for a weak resonance line. The hump in the $3p$ curve is due to optical pumping in $3p$–$2s$

has been included using the classical hydrogenic formula (e.g., Unsold 1955) with a multiplicative factor of 1.5 (Andretta et al. 1991). It is significant only for the cooler models. Stark broadening is included according to Dimitrijevic & SahalBrechot (1991) but does not contribute significantly to the line width.

The effects of uncertainties in the atomic data on the results are discussed in Sect. 5.

4. Results

4.1. Lithium line formation in the young sun

Figure 4 shows results for the populations of solar Li I levels when the lithium abundance is increased from the current solar value of $A_{\rm Li} \approx 1.1$ to the meteoritic value $A_{\rm Li} = 3.3$. This increase portrays lithium line formation in the young sun before lithium depletion took place, on the assumption that the photospheric stratification has remained the same. It is a better model for studying lithium line formation in solar-type lithium-rich stars than the present sun, in which the lithium lines are so weak that the background continuum processes dominate the kinetic equilibrium even for the resonance lines.

The coefficients β_i plotted along the ordinate in Fig. 4 measure non-LTE population departures n_i/n_i^*, where n_i is the actual population of a level i and n_i^* the LTE population computed from the Saha and Boltzmann distributions. They are defined by Wijbenga & Zwaan (1972) and differ from the more commonly used Menzel b coefficients (Menzel & Cillie 1937) in their normalization. The β coefficients are relative to the lithium abundance, whereas the b coefficients are normalized by the number density of the Li II ion. For Li I the b_i and β_i values are approximately the same wherever lithium is predominantly ionized, which is the case for all photospheres in our model grid.

The line extinction coefficient scales approximately with the value of β_l for the lower level of a bound-bound transition, whereas the line source function S_l scales approximately with the upper/lower coefficient ratio β_u/β_l. These dependences are exact in the Wien part of the spectrum, for negligible stimulated emission. Since the emergent stellar surface flux F_ν is given in the Eddington-Barbier approximation by $F_\nu \approx S_\nu(\tau_\lambda = 2/3) \approx (\beta_u/\beta_l)B_\nu(\tau_\lambda = 2/3)$, non-LTE absorption line strengthening occurs both for $\beta_l > 1$ and for $\beta_u < \beta_l$. In the first case, the larger line opacity causes larger formation height where the line samples a lower value of the source function; in the second case, the line source function S_l drops further below the local Planck function B_ν.

Figure 5 shows the line source function S_l for Li I 670.8 nm ($2p$–$2s$) in the young sun together with the Planck function B_ν at that wavelength (dashed). The line has $S_l > B_\nu$ in the deep photosphere where $\beta_{2p} > \beta_{2s}$, and $S_l < B_\nu$ above lg $\tau_{500} \approx -0.8$. The vertical arrow marks the separation between B_ν and S_l at the location (marked by a square) where the optical depth at line center reaches unity (cf. upper inset scale of Fig. 4). This depth is shifted slightly outward from the LTE optical depth

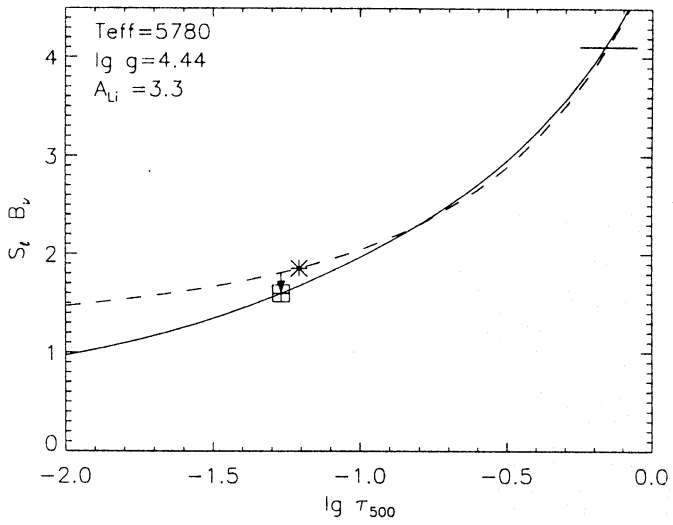

Fig. 5. Young-sun Planck function B_ν (dashed) and non-LTE Li I line source function S_l (solid) at λ = 670.8 nm against the logarithm of the continuum optical depth at λ = 500 nm. The dash at upper right cuts the B_ν curve at the location of continuum optical depth unity for λ = 670.8 nm, while the square mark on the S_l curve marks the location with total optical depth unity; the part of the S_l curve between dash and square maps into the emergent line profile. The vertical arrow indicates the LTE to non-LTE source function difference at the height of line formation. Its length corresponds to the local divergence between the $2p$ and $2s$ departure coefficients in Fig. 4, which is controlled by the resonance line $2p$–$2s$. The asterisk marks the location where the total LTE opacity at λ = 670.8 nm equals unity. Its horizontal shift from the square mark is set by the $2s$ departure coefficient in Fig. 4. Ordinate units: 10^5 erg cm^{-2}s^{-1}ster^{-1}Hz^{-1}

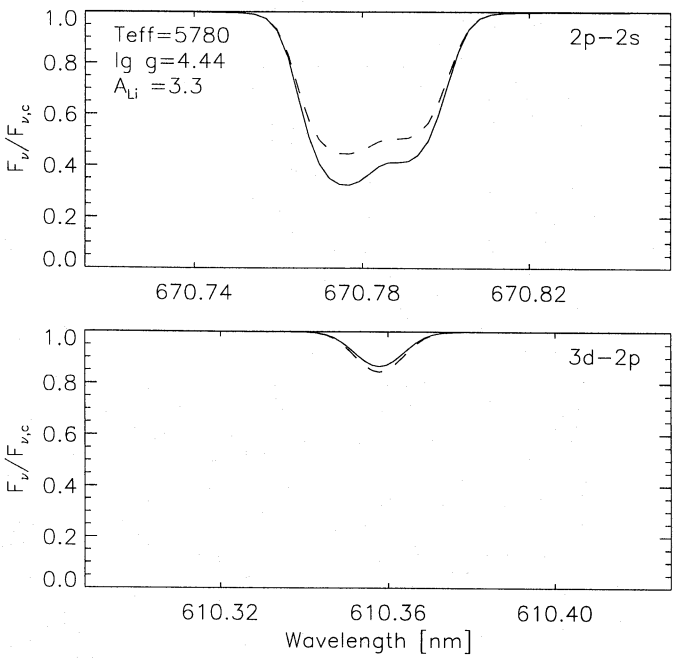

Fig. 6. Young-sun emergent profiles of the Li I 670.8 nm doublet (upper panel) and the Li I 610.4 nm subordinate line (lower panel). Ordinate: surface flux relative to the continuum. Abscissa: wavelength in nm. Dashed: LTE modeling. Solid: non-LTE modeling. For the resonance line, both the non-LTE line source function correction and the non-LTE line opacity correction cause line strengthening whereas the two corrections compete for the subordinate line (cf. Fig. 5). The weak blends from the ^{6}Li isotope have been neglected and no macroturbulent or rotational broadening has been applied

unity location, marked with an asterisk on the B_ν curve, because β_{2s} has a hump exceeding unity just above this height (Fig. 4).

We show the corresponding emergent flux profiles in Fig. 6. The upper panel, for the 670.8 nm doublet, illustrates that the non-LTE computation (solid) gives an appreciably deeper line than the LTE one because both the $S_l < B_\nu$ source function departure and the $\beta_{2s} > 1$ opacity departure cause line strengthening. In contrast, the two corrections compete for the subordinate $3d$–$2p$ line at λ = 610.4 nm which is shown in the lower panel. Its source function correction β_{3d}/β_{2p} produces $S_l < B_\nu$ line strengthening, but its β_{2p} opacity correction works the other way (cf. Fig. 4). The non-LTE modeling gives a slightly weaker line than the LTE result.

Figures 4–6 display non-LTE corrections for the Li I lines from the young sun, but they do not explain how the departures arise. In general, it is not easy to identify the processes which cause non-LTE effects from such plots. They show the eventual results when overall kinetic equilibrium is reached (in the computer), but they do not show which processes drive the departures and which processes constitute the loop closing that is necessary for equilibrium. Such process identification requires further diagnostics, for example as given by Bruls et al. (1992) for the solar K I and Na I spectra and by Carlsson et al. (1992a) for the solar Mg I Rydberg lines. We take this approach in the remainder of this section, aiming to use young-sun lithium line formation as a basis for understanding the stellar results in Sect. 4.3 without having to analyze the latter star by star. We discuss them in the order of the mechanism list of Sect. 2.

Resonance line formation. Figure 4 shows a pattern for β_{2s} with an initial hump, a dip, a higher hump and a steep decline for decreasing optical depth τ_{500}, whereas the β_{2p} curve displays a decline only. Together, these two curves describe the formation of the 670.8 nm resonance doublet. How do they come about?

Figure 7 provides diagnostics. The upper panel displays the net radiative rate and the net collision rate in the $2p - 2s$ resonance transition, with upward net rate positive. The net radiative rate (unmarked curve) has, from right to left, a negative dip, a positive hump and another negative dip of which the zero crossings correspond to the cross-over locations of the $2p$ and $2s$ curves in Fig. 4. In the first dip the photodeexcitation rate exceeds the absorption rate, so that the $2s$ level builds up overpopulation. The hump consists of overexcitation by photons, reducing the $2s$ departure coefficient while increasing the $2p$ one. The second dip, above lg $\tau_{500} = -0.7$, results again in increase of β_{2s} relative to β_{2p}. The amplitudes of these height variations in the $2s$–$2p$ net radiative rate and the β_{2p}/β_{2s} ratio differ because the net rates decrease outward with the electron density decrease, whereas the resulting departures increase out-

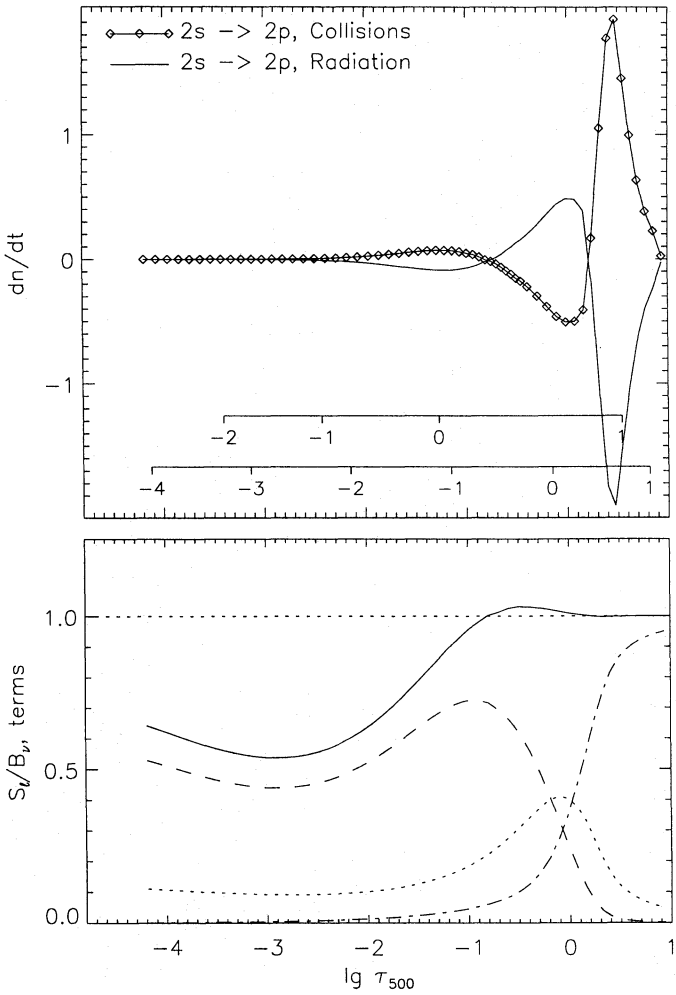

Fig. 7. *Upper panel:* Net rates in the $2p$–$2s$ transition against optical depth. The inset optical depth scales are for continuum and line center, as in Fig. 4. The net rates are given in units of 10^{10} transitions per second; positive values specify excess of upward over downward rates. Unmarked curve: net upward radiative rate. Marked curve: net upward collision rate.
Lower panel: Ratio of the 670.8 nm line source function to the Planck function S_l/B_ν (solid) and its three contributions (cf. eq. 1): $(1-\varepsilon)\overline{J}_l/B_\nu$ due to resonance scattering (dashed curve), $(1-\varepsilon)\overline{J}_c/B_\nu$ due to photons from the background continuum (dotted), ε due to collisional excitation (dot-dashed)

ward since they are measured as population fractions. The two patterns correspond, however.

The marked curve in Fig. 7 is for the net collision rate. It shows an identical pattern but upside down. This implies that the source function of the 670.8 nm resonance line obeys the two-level approximation closely. If the upper or lower level populations are out of LTE, the collisional transitions between them match the resulting imbalance when kinetic equilibrium is reached so that the total net rate remains close to zero. In other words, the ratio of the $2p$ and $2s$ populations is not very sensitive to other Li I non-LTE photon processes than those in the resonance line itself. In particular, there is only slight sensitivity to bound-free Li I continuous processes; these affect the line opacity more than the line source function.

What are the non-LTE processes in the 670.8 nm line? These are specified in the lower panel of Fig. 7. This is a graphical formulation of the two-level line source function in the presence of an overlapping background continuum. The latter is important since the 670.8 nm line is only a weak resonance line. The line source function S_l may be split into three constituents according to

$$S_l = (1-\varepsilon)\overline{J}_l + (1-\varepsilon)\overline{J}_c + \varepsilon B_\nu \tag{1}$$

where B_ν is the Planck function to which the continuum source function S_c is equal, and ε the collisional photon destruction probability given by

$$\varepsilon = \frac{C_{ul}}{A_{ul}+C_{ul}}, \tag{2}$$

neglecting stimulated emission, with A_{ul} and C_{ul} the Einstein probabilities for radiative and collisional deexcitation from the upper level u to the lower level l. We define the two angle-averaged and profile-averaged radiation fields $\overline{J}_l$ and $\overline{J}_c$ through lambda operations on the profile-weighted line and continuum source functions:

$$\overline{J}_l \equiv \Lambda\left[(1-r_\nu)S_l\right] \tag{3}$$

$$\overline{J}_c \equiv \Lambda\left[r_\nu S_c\right] \tag{4}$$

in which $r_\nu = \alpha_c/\alpha_l$ is the ratio of the extinction from background continuum processes α_c to the line extinction α_l, and Λ is the lambda operator (e.g., eq. (2-58) of Mihalas 1978). The total source function is given by $S = (r_\nu S_c + S_l)/(1+r_\nu)$ or $S \approx (1-r_\nu)S_l + r_\nu S_c$ for $\alpha_l \gg \alpha_c$.

We have determined the radiation fields $\overline{J}_l$ and $\overline{J}_c$ numerically by applying the above lambda operations using our computed values of r_ν, S_l and $S_c = B_\nu$ as a function of optical depth. They are equivalent to the two integrals in eq. (2.25) of the analytical formulation of this problem by Hummer (1968) for the case of depth-independent r_ν and line profile shape, which is also presented on pp. 350–352 of Mihalas (1978). Mihalas' eq. (11-46) is the same as Hummer's eq. (2.25) and corresponds to our eq. (1) above. The interpretation of the three terms in eq. (1) is straightforward and given after eq. (2.27) by Hummer and after eq. (11-51) by Mihalas, respectively. The term $(1-\varepsilon)\overline{J}_l$ specifies the contribution of photons in the line due to resonance scattering. The term $(1-\varepsilon)\overline{J}_c$ describes photons that are fed into the line by continuum background processes at the same wavelength, primarily radiative recombination of H^-. The term εB_ν measures the production of photons that are created by collisional excitation.

The three terms are plotted in the lower panel of Fig. 7 as contributions to the ratio S_l/B_ν. These curves enable identification of the causes for the pattern in the upper panel. As usual, the destruction probability ε (dot-dashed curve) drops steeply with height above the thermalization depth where $\varepsilon \approx 1$, which is located well below $\tau_\nu = 1$ in the continuum. The relative contribution of thermally created photons, which dominates the line

source function at large depth, follows this steep outward decline. In the deepest layers its decline is matched by an increase of photon creation from H^- recombination (dotted curve), of which the contribution peaks at the height where the continuum has optical depth unity and the line is yet opaque. The combination of reduced photon destruction and increasing continuum contribution causes the initial downturn of the net radiative rate in the upper panel. It reverses into an upturn where resonance scattering begins to contribute because this process does not produce new photons but uses existing ones. The summation of the three processes causes a hump of net upward radiative rate in the upper panel which translates into a hump with $S_l > B_\nu$ in the lower panel. Above this height, all three contributions diminish outward. The decline of the scattering contribution, which is the dominating contribution, is due to photon losses in the line. They set in already below the optical depth unity location $\lg \tau_l = 0$ because ε is already small at that height. Finally, towards the top of the atmosphere the two radiative contributions increase slightly. This is because the Planck function B_ν decreases outward (Fig. 1), whereas the radiation fields $\overline{J}_l$ and $\overline{J}_c$ remain constant with height at this altitude. The resulting outward increase of S_l/B_ν corresponds to the outward convergence of the $2s$ and $2p$ curves in Fig. 4.

Photon suction. The opacity of the resonance line, set by β_{2s}, is not only sensitive to the net rates within the $2p$–$2s$ transition but also to the ionization equilibrium and its own influence on all levels. At the young-sun lithium abundance, the line is strong enough that its photon losses drive some recombination from Li II in the form of photon suction. It causes the bulge in β_{2s} around $\lg \tau_{500} = -2$, which just exceeds unity and therefore causes the slight leftward shift, between asterisk and square, of the line-center optical depth unity locations in Fig. 5.

Overionization. The general outward downslope of the β_i curves in Fig. 4 is due to overionization, primarily from the $2p$ level. This process is illustrated by Fig. 8. The upper panel shows a spread of characteristic angle-averaged radiation fields J_ν as sampled by frequencies in the $2p$ bound-free continuum edge. The differences between the curves stem from the rapid opacity variations of the ultraviolet line haze, shown in the lower panel for the height where the 670.8 nm line is formed. The peaks in J_ν are appreciably higher than the local Planck function (thick curve). The resulting underpopulation of $2p$ is large enough that the corresponding opacity decrease outweighs the non-LTE source function enhancement for the 610.4 nm subordinate line (Fig. 6).

Overrecombination. Extra recombination that is driven by line photon losses and ultraviolet pumping comes down primarily along high levels, where a net Rydberg diffusion flow increases to accommodate more recombination through larger departure divergences between adjacent levels (cf. the case of Mg I as studied by Carlsson et al. 1992 and illustrated by Rutten & Carlsson 1994). The precise details of this flow are not important for the

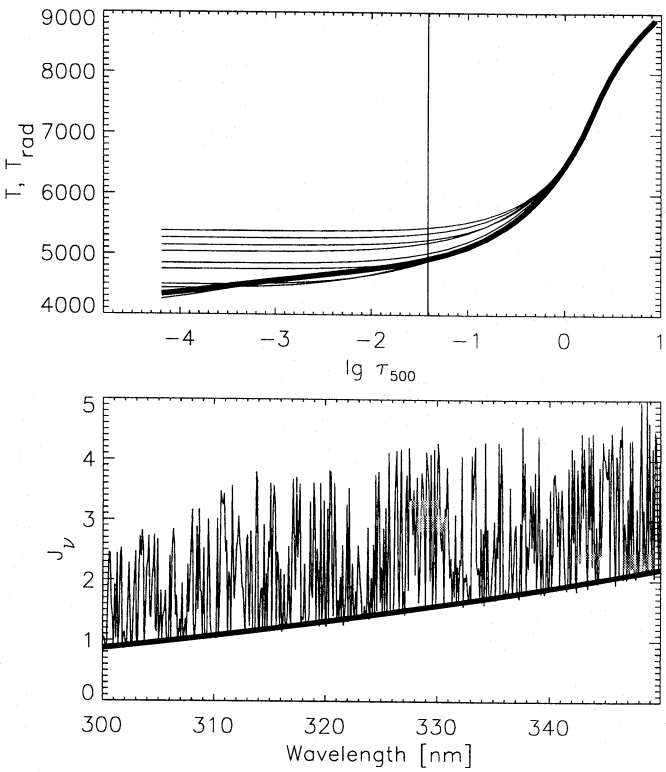

Fig. 8. Radiation fields in the solar atmosphere near the Li I $2p$ photoionization edge at λ = 349.8 nm. *Upper panel:* radiation temperatures as a function of optical depth. The thick curve is the electron temperature and represents a Planckian radiation field $I_\nu = J_\nu = B_\nu$. The other curves represent the angle-averaged mean intensity J_ν for wavelengths just short of the $2p$ edge, that are selected to sample variation in background line-haze opacity. The vertical line indicates the mean depth of formation of the Li I 670.8 nm line.
Lower panel: mean intensity J_ν as a function of wavelength, for the optical depth marked in the top panel. The edge wavelength is at right. The thick curve is the Planck function. At wavelengths where the line haze is opaque $J_\nu \approx S_\nu = B_\nu$. The highest peaks between lines correspond to the top J_ν curve in the top panel. These peaks produce non-LTE overionization. Ordinate units: 10^6 erg cm^{-2}s^{-1}ster^{-1}Hz^{-1}

formation of the observable lithium lines, as long as the model atom has levels that are sufficiently close to the continuum that the replenishment recombination is maintained without requiring enhanced underpopulation of low-lying levels as would be the case for model atoms of too limited extent.

Bound-bound pumping. The β_{3p} curve in Fig. 4 deviates markedly from the other excited levels due to photon pumping in the $3p$–$2s$ transition. The corresponding bulge sits so high in the atmosphere that it does not influence the observable lithium lines, nor does it couple collisionally to the close-lying $3d$ level.

4.2. Solar non-LTE corrections

Figures 9 and 10 show the young-sun non-LTE results in formats habitually employed in stellar abundance analysis. Figure 9 shows curves of growth for Li I 670.8 nm and Li I 610.4 nm. At

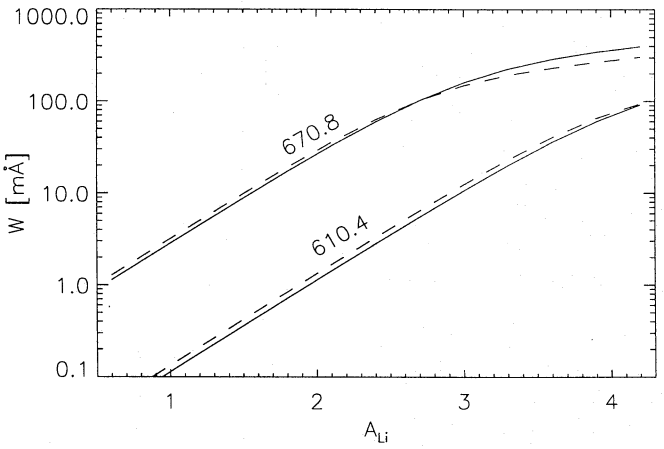

Fig. 9. Solar curves of growth for Li I 670.8 nm (upper pair of curves) and Li I 610.4 nm (lower pair). Abscissa: input value of the lithium abundance $A_{\rm Li} = \lg(n_{\rm Li}/n_{\rm H}) + 12$. Ordinate: computed equivalent width in mÅ. Solid: non-LTE results. Dashed: LTE results

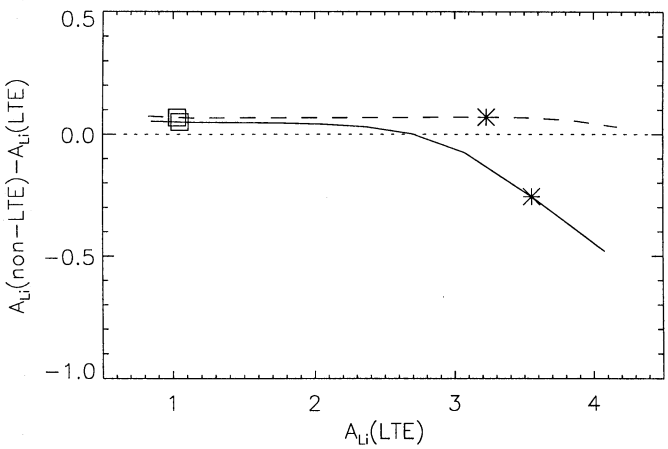

Fig. 10. LTE to non-LTE abundance corrections for solar lithium, respectively for the 670.8 nm resonance line (solid) and the 610.4 nm subordinate line (dashed). The LTE abundance is plotted along the abscissa; this is the value one obtains from our non-LTE computed lines by fitting their equivalent width with LTE line formation using the same atmospheric model. The ordinate measures the corrections that should be added to such LTE estimates to obtain the correct non-LTE abundance. The star on each curve marks the meteoritic lithium abundance $A_{\rm Li} = 3.3$ used here for young-sun modeling. LTE abundance analysis of the Li I 670.8 nm line from the young sun would have overestimated its actual lithium abundance by 0.26 dex (a factor 1.8). For lithium-rich suns, the Li I 610.4 nm line is a much better LTE estimator, with an error of only 0.07 dex of opposite sign. The squares mark the present solar abundance $A_{\rm Li} = 1.1$

low abundance, the LTE curves nearly equal the non-LTE ones, with a slight excess of the LTE-computed equivalent width W due to the neglect of overionization. The resonance-line effects discussed above are less important for small lithium abundance. At large abundance, the Li I 670.8 nm curves show appreciable difference, with the LTE computation in deficit. The deficit starts at $A_{\rm Li} \approx 2.7$ where the line also starts to saturate. At $A_{\rm Li} = 3.3$ the deficit corresponds to the profile difference shown in the upper panel of Fig. 6. It increases further towards larger abundance.

The saturation of the 670.8 nm line enhances the LTE deficit when measured horizontally, i.e., in the form of an abundance correction. This is demonstrated in Fig. 10 which shows LTE to non-LTE corrections applicable to LTE line synthesis. The abscissa specifies the LTE abundance $A_{\rm Li}^{\rm LTE}$ that would be derived through fitting our non-LTE-computed line profile assuming LTE. The ordinate measures the difference with the actual input non-LTE value $A_{\rm Li}$. Thus, this graph is a direct representation of the required correction. The 670.8 nm curve drops steeply where the line saturates, reaching $A_{\rm Li} - A_{\rm Li}^{\rm LTE} \approx -0.5$ dex at right. This drop is due to the effects of resonance scattering on both the line source function and the line opacity, as analyzed above. At left, for small lithium abundance, both lines show only the effect of overionization which requires positive corrections smaller than 0.1 dex. The curve for the 610.4 nm remains flat towards larger $A_{\rm Li}^{\rm LTE}$ because, while the line forms at larger height, it samples both a larger non-LTE opacity decrease (downslope of β_{2p} in Fig. 4) which weakens the line, and increasing source function deficit β_{3d}/β_{2p} which strengthens the line. The two effects compensate each other.

4.3. Lithium line formation across the cool-star grid

We now turn to the formation of lithium lines in all models of our grid of cool-star atmospheres. For each of them, we have inspected graphs as shown for the young sun in the previous sections. There are fairly complex model-to-model variations. The differences in temperature and electron density stratifications shown in Figs. 1 and 2 produce large variation in the partitioning between Li I and Li II, in the resonance-line effects, in the competition between $2p$ and $2s$ photoionization, in the effects of metallicity, etc. The patterns that are present in Figs. 4–8 therefore change appreciably across the grid. It is impractical to display these for each model and for each abundance value separately. We have therefore chosen to display line formation graphs only for the young-sun abundance value of $A_{\rm Li} = 3.3$, and to do so only for an illustrative subset of the model grid. These displays are given in Figs. 11–14. They share the same panel layout to facilitate comparisons.

The model selection from the grid in Figs. 11–14 is the same as in Figs. 1 and 2, but the panel layout differs because the models are now split in metallicity, respectively [Fe/H] = 0 for the lefthand columns and [Fe/H] = −2 for the righthand ones. The results for dwarfs ($\lg g = 4$) are shown in the upper six panels, for giants ($\lg g = 0$) in the lower four.

Each panel in Fig. 11 is a graph comparable to the solar one in Fig. 4; likewise, each panel in Fig. 12 is comparable to Fig. 5 and each panel in Fig. 13 is comparable to the lower panel of Fig. 7. In particular, the second panels in the lefthand columns (those with $T_{\rm eff} = 6000$ K, $\lg g = 4$ and [Fe/H] = 0) correspond closely to the young-sun results, as indicated by the proximity of the corresponding models in Figs. 1 and 2. We discuss these solar-like models first in order to extend the interpretation in

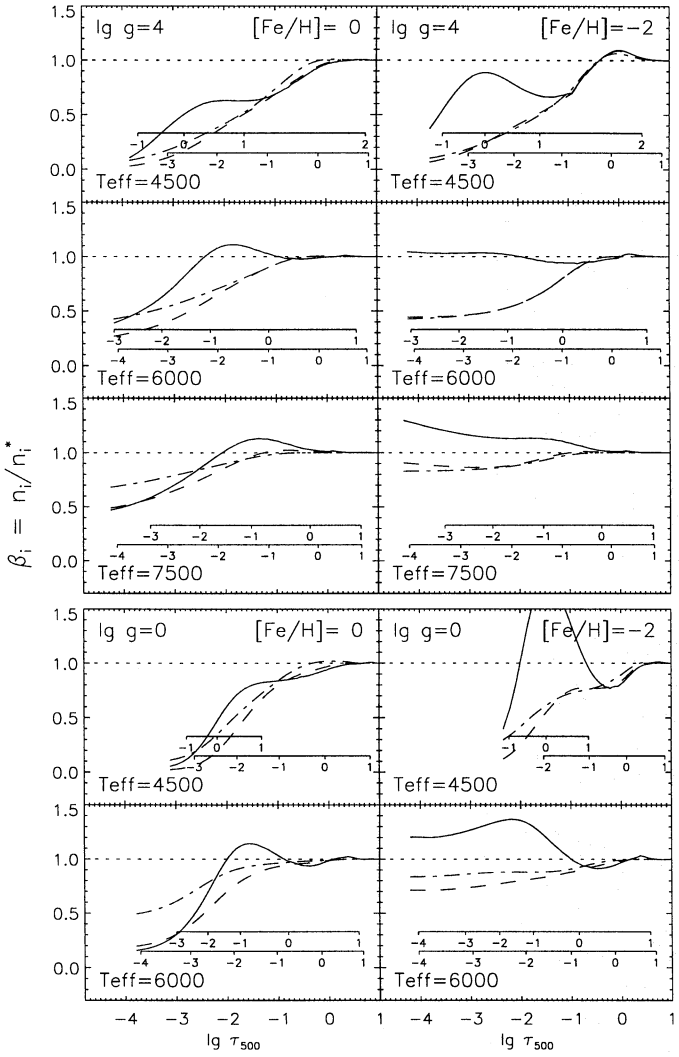

Fig. 11. Non-LTE population departure coefficients $\beta_i = n_i/n_i^*$ for selected grid samples, for $A_{\rm Li} = 3.3$. The model samples are the same as in Figs. 1 and 2. They are here split into [Fe/H]=0 lefthand panels and [Fe/H]=-2 righthand panels. The upper portion, with six panels, contains the lg $g = 4$ models while lg $g = 0$ for the bottom four panels. Each panel is a plot as Fig. 4, but only for the levels $2s$ (solid), $2p$ (dashed) and $3d$ (dot-dashed) which govern the 670.8 nm and 610.4 nm lines. Axis labeling and inset scales as in Fig. 4

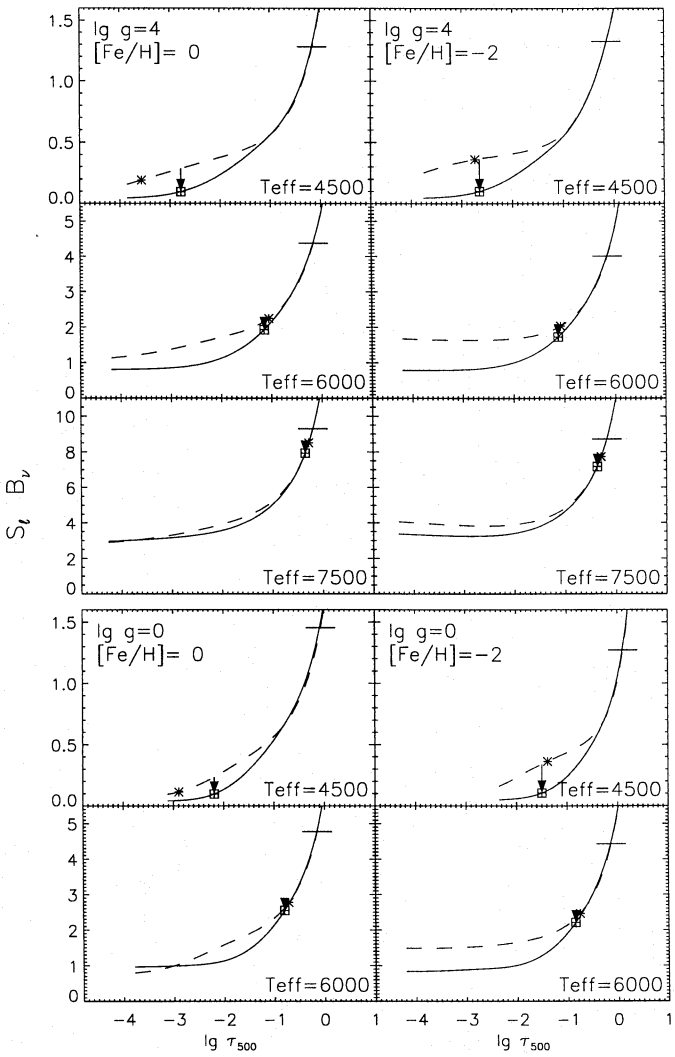

Fig. 12. Planck functions (dashed) and Li I line source functions (solid) at $\lambda = 670.8$ nm against the logarithm of the continuum optical depth at $\lambda = 500$ nm. The grid sampling and panel layout are the same as in Fig. 11. Axes, curve coding and marks as in Fig. 5; the marks are again for lithium abundance $A_{\rm Li} = 3.3$

Sect. 4.1 with the results for the case of a comparable solar-type dwarf of low metallicity shown in the opposite panels (second panels in righthand columns).

Figure 14 does not have a solar analog in Sect. 4.1. Each panel of this figure results from a "multi-MULTI" analysis in which MULTI was run many times to test the sensitivity of the converged solution to changes in input parameters. In a full multi-MULTI run the effect of each input parameter (oscillator strength, collision cross-section, photoionization cross-section, etc.) is studied by taking the resulting change in an important quantity as gauge. That quantity is monitored while all input parameters are changed one at a time. In Fig. 14, we use the multi-MULTI results to study photoionization. Each panel shows the fractional change of the $2p$ population due to changes in the various cross-sections for photoionization. The solid curves are the change in $2p$ population due to doubling of the $2s$ bound-free cross-section $\alpha_{2s}^{\rm bf}$, the dashed curve is for doubling $\alpha_{2p}^{\rm bf}$ itself, the other curves (all dotted) are for doubling the cross-sections for photoionization from higher levels.

The interpretation of the multi-MULTI results for the solar-like model in Fig. 14 (second panel of lefthand column) is straightforward: the $2p$ population decreases when ionization from either $2s$ or $2p$ increases. The sensitivity to $\alpha_{2p}^{\rm bf}$ starts deeper because the radiation fields in the $2p$ edge originate in deeper layers (cf. Fig. 8). The higher levels are much less important; increasing their photoionization cross-sections causes slight increase of the $2p$ population for transitions with net recombination.

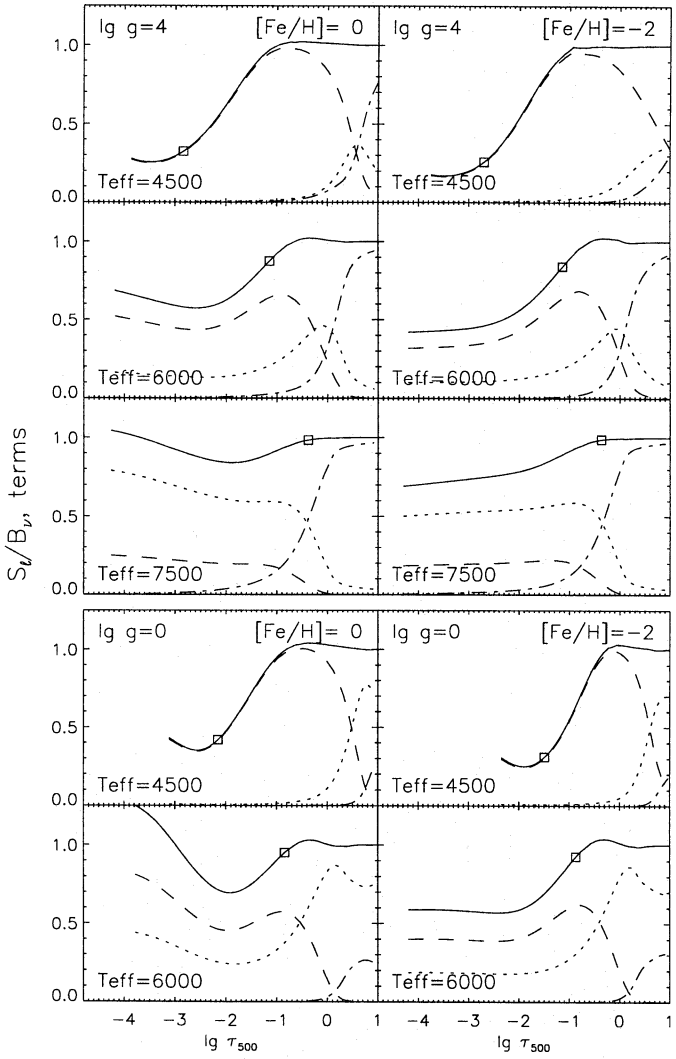

Fig. 13. Ratio of the 670.8 nm line source function to the Planck function S_l/B_ν (solid) and the contributions by resonance scattering (dashed), background continuum processes (dotted) and collisional excitation (dot-dashed) for lithium abundance $A_{\rm Li}$ = 3.3. The square marks the location where the line center optical depth is unity. The grid sampling and panel layout are the same as in Fig. 11. Axes and curve coding as in the lower panel of Fig. 7

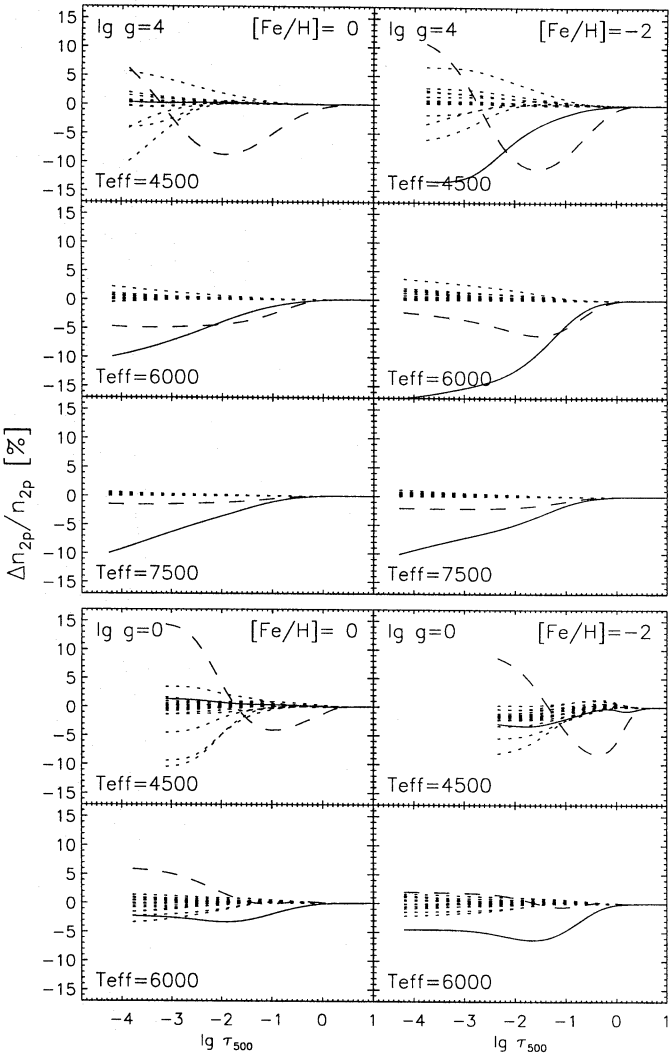

Fig. 14. Results from "multi-MULTI" sensitivity computations for lithium abundance $A_{\rm Li}$ = 3.3. Each panel shows the percentage change of the $2p$ population density $\Delta n_{2p}/n_{2p}$ when various photoionization cross-sections $\alpha_i^{\rm bf}$ are doubled one by one. Curve coding: effect on n_{2p} from doubling the photoionization from $2s$ (solid), from $2p$ (dashed), and from higher levels (all dotted). The grid sampling and the panel layout are the same as in 11. Photoionization from $2p$ dominates in cool stars, while photoionization from the ground level ($2s$) becomes more important with increasing effective temperature. Line blocking kills the photoionization from $2s$ at high metallicity and low effective temperature. The upturn of the $2p$ curves in the $T_{\rm eff}$ = 4500 K panels is caused by photon losses in the $2p$–$2s$ resonance which draw replenishment recombination from Li II

At low metallicity (second panel in the righthand column of Fig. 14), the effect of doubling $\alpha_{2s}^{\rm bf}$ is much larger because the $J_c > B_\nu$ radiation excess grows when the ultraviolet line blocking is reduced, even though B_ν then has a shallower gradient in the outer layers due to less blanketing (middle lefthand panel of Fig. 1). The initial dip of the $2p$ sensitivity curve is deeper than at left for the same reason, but at larger height this curve turns up slightly towards smaller change. This upturn is due to the combination of the model temperature flattening shown in Fig. 1 and the reduction in electron density shown in Fig. 2. The temperature flattening reduces the $J_c - B_\nu$ excess (cf. Fig. 8), while smaller electron density enhances the efficiency of photon losses in the resonance line to drive replenishment recombination from the continuum. The latter driving is more important than overionization from $2p$ in higher layers, and also causes the flattening of the $2p$ curve in the lefthand panel.

The effect of this metallicity sensitivity of lithium populations in solar-like dwarfs is seen when comparing the lefthand and righthand panels in the second row of Figs. 11–13. The β_{2p} curve initially dives faster for low metallicity due to larger, unblocked $J_c - B_\nu$ excess, but it flattens out at larger height due to the temperature flattening and the increased photon-loss-driven

recombination from Li II. The β_{2s} curves flattens even more, losing its steep outward drop in the lefthand panel altogether, because the model temperature flattening also reverses the slope of the S_l/B_ν ratio in high layers (cf. Figs. 12 and 13). The ratio equals the split between the β_{2s} and β_{2p} curves in Fig. 11.

Figure 12 shows that these metallicity changes have virtually no significance for the formation of the 670.8 nm line from solar-type dwarfs. The largest effect is a slight drop in emergent continuum intensity due to smaller line blanketing. This is confirmed by the profiles shown in the next section (Fig. 15). However, the sensitivity to metallicity increases for larger lithium abundance than the young-sun value.

Let us now turn to the non-solar models in the other panels of Figs. 11–14. The first thing to note is the large variation in height of line formation due to trends in the ionization equilibria. These height variations are evident from comparing the line-center optical depth unity locations (upper inset scales in Fig. 11) and from comparing the τ_{500} locations of the squares in Fig. 12. The asterisks on the Planck functions (dashed curves in Fig. 12) show the trends in LTE Saha-Boltzmann partitioning. The LTE line opacity diminishes rapidly with increasing $T_{\rm eff}$ (vertically along columns) and diminishes also with decreasing electron density (shifts between $\lg g = 4$ and corresponding $\lg g = 0$ panels). The latter dependency also causes the substantial 670.8 nm opacity decrease between high and low metallicity in cool stars (horizontally along rows). It is due to the large divergence between the solid and dashed curves in the $T_{\rm eff} = 4500$ panels of Fig 2. This shift is larger for giants than for dwarfs.

These large variations in the opacity of the 670.8 nm resonance line are reflected in the balancing of the contribuants to its source function, shown in Fig. 13. In cool stars, resonance scattering dominates already in deep layers; the two-level approximation is fully valid at the height of line formation. The contributions from continuous and collisional photon creation drop much faster for $T_{\rm eff} = 4500$ than in the solar case; the second contribution is negligible even at large depth in the case of cool giants. With increasing effective temperature the balance shifts appreciably. In the $T_{\rm eff} = 7500$ panels, continuum photon creation and collisional photon creation contribute about equally at the height of line formation, while resonance scattering contributes only marginally at all heights. The $T_{\rm eff} = 6000$ panels provide similar patterns as in Fig. 7, with a different split between continuous and collisional photon creation in the deepest layers for dwarfs and giants.

The different constitution of the S_l/B_ν ratio along columns in Fig. 13 is also evident in Fig. 12 in the shift of the location of the squares relative to the size of the non-LTE divergence between S_l and B_ν. For the cool stars, the combination of photon losses and resonance scattering causes the 670.8 nm line to be formed at heights where S_l is fully detached from B_ν; for these, scattering presents a photon leak towards outer space well below optical depth unity in the line. In contrast, in the $T_{\rm eff} = 7500$ panels the line is largely formed below the height where S_l/B_ν departs from unity. This is reflected in Fig. 11, in which the departure coefficients are close to unity at the line center formation depth for the warmer atmospheres.

The Saha-Boltzmann variations also influence the non-LTE part of the ionization balance, and therefore the non-LTE part of the 670.8 nm opacity. The resonance line is quite strong in the coolest stars; its photon losses drive large replenishment recombination from the continuum in higher layers. This is seen when comparing $2s$ curves between lefthand and righthand $T_{\rm eff} = 4500$ panels in Fig. 11, most conspicuously for the giants in the lower block. These have the largest drop in electron density from metal rich to metal poor (Fig. 2). The drop causes considerable reduction of the LTE opacity of the 670.8 nm line (shift for the corresponding asterisks in Fig. 12), but also large enhancement of the photon-loss dominated S_l/B_ν deficit (arrow length in Fig. 12). The source function deficit translates in wide divergence between the β_{2s} and β_{2p} curves in the metal-poor case. However, these photon losses do not result in reduction of the $2p$ population, but rather in a high peak in β_{2s} at the location where the line optical depth reaches unity. This is the photon suction effect: the photon losses are replenished by recombination from the reservoir in Li II. For the cool stars, they take over the role of dominant driver of non-LTE departures in the ionization balance from $2p$ overionization at the line-center optical depth unity location.

The effect of such replenishment recombination is also seen in the upturns of the $2p$ sensitivity curves in the $T_{\rm eff} = 4500$ panels of Fig. 14. They are centered on the line-center optical depth unity locations and mark the regime where the $2p$ population departure is no longer dominated by ultraviolet overionization, but by drawing sufficient recombination down from the continuum to make up for resonance-line photon losses. The same condition causes the $2p$ curves in the lefthand and righthand $T_{\rm eff} = 4500$ panels of Fig. 11 to be about the same even though the $2s$ curves differ markedly. The $J_c > B_\nu$ radiation excess then produces appreciably more net ionization from $2p$ when $\alpha^{\rm bf}_{2p}$ is doubled. It adds more overall recombination to the amount already required by the resonance-line photon losses. Since the recombination comes down primarily along higher levels than $2p$, the $2p$ population itself does not necessarily decrease when $\alpha^{\rm bf}_{2p}$ increases, and may even grow along with the total Li I population.

For the giants in the $\lg g = 0$ panels of Fig. 11, the combined effect is to produce substantial overpopulation of the whole neutral Li I stage around optical depth unity in the line. In Fig. 12 this overpopulation reverses the asterisk-to-square LTE to non-LTE shift between the lefthand panel and the righthand panel ($T_{\rm eff} = 4500$ and $\lg g = 0$). This reversal reduces the very large horizontal shift between the two LTE asterisks to a smaller one between the two non-LTE squares.

4.4. Stellar non-LTE corrections

Figure 15 shows computed profiles for the 670.8 nm line, again for the grid selection of Fig. 11 and with the same panel layout. There are profiles for three characteristic values of the lithium abundance, the higher one ($A_{\rm Li} = 3.3$) corresponding to the young-sun value used in Sects. 4.1 and 4.3. The differences between the various panels correspond directly to

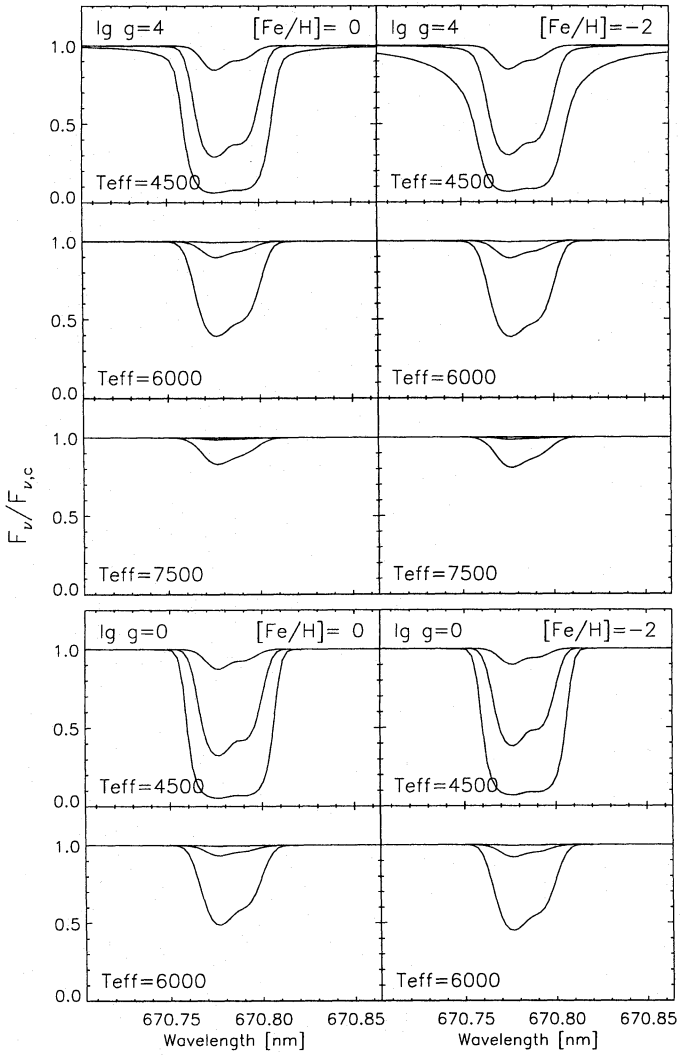

Fig. 15. Computed stellar Li I 670.8 nm line profiles. The grid sampling and panel layout are the same as in Fig. 11. Axes as in Fig. 6. Each panel contains profiles for $A_{\rm Li}$ = 0.9, 2.1 and 3.3. The weak blends from the ^{6}Li isotope have been neglected and no macroturbulent or rotational broadening has been applied

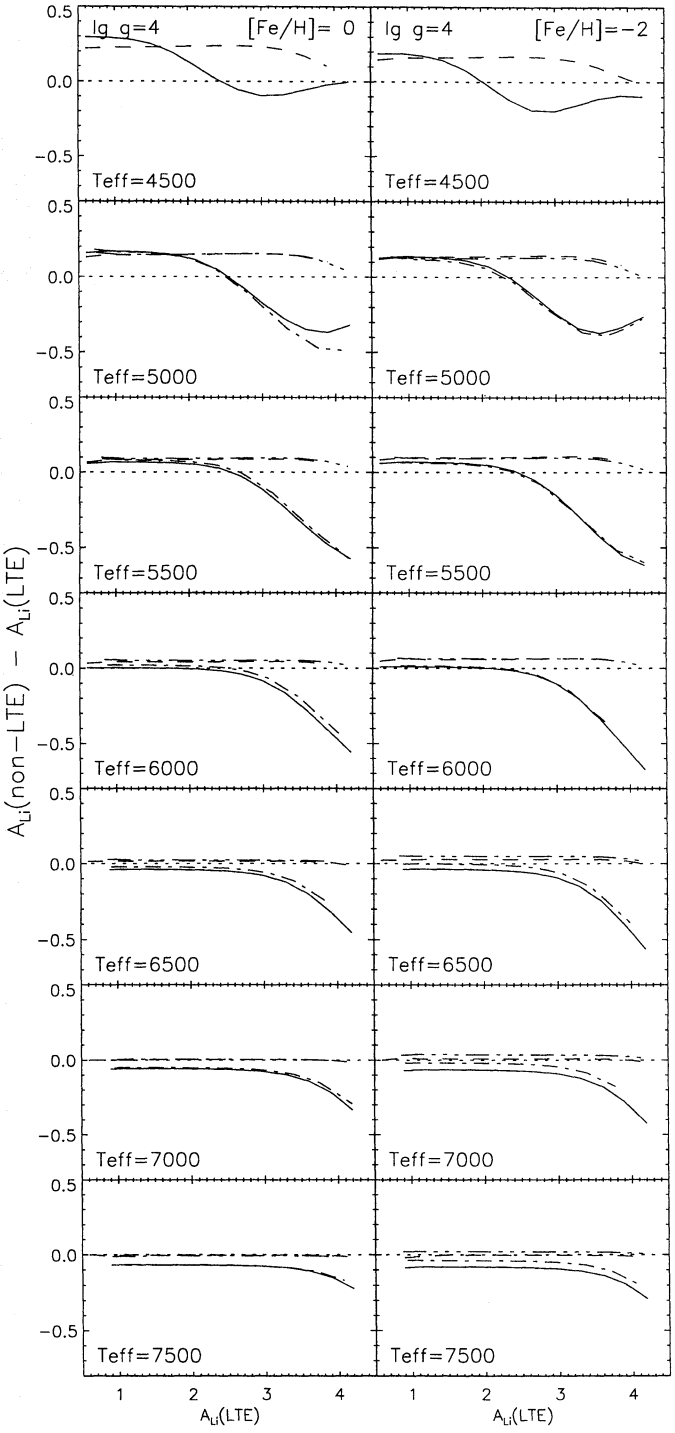

Fig. 16. LTE to non-LTE lithium abundance corrections for dwarfs (lg g = 4), respectively for the Li I 670.8 nm resonance line (solid) and the Li I 610.4 nm subordinate line (dashed). Each panel is a plot as Fig. 10, for a model from the grid as specified. Dot-dashed curves are for opacity sampling (Sect. 5)

the formation characteristics displayed in Fig. 12, which summarizes the source function and opacity effects analyzed in Figs. 11, 13 and 14.

The most obvious change in emergent line profile is along columns, due primarily to Saha-Boltzmann partitioning. There is not much qualitative difference in the emergent profiles between metal-rich stars (lefthand panels) and metal-poor stars (righthand panels). For the cool stars, where large metallicity differences are seen in the β_{2s} curves of Fig. 11, the close agreement stems from fortuitous cancellations between the influence of the β_{2s} differences on the line opacity and on the line source function, and also between the changes in temperature stratification and the lowering of the emergent continuum flux for smaller metallicity.

For example, the $T_{\rm eff}$ = 4500 profiles for giants (lg g = 0) are about the same at $A_{\rm Li}$ = 3.3 in the left and righthand panels

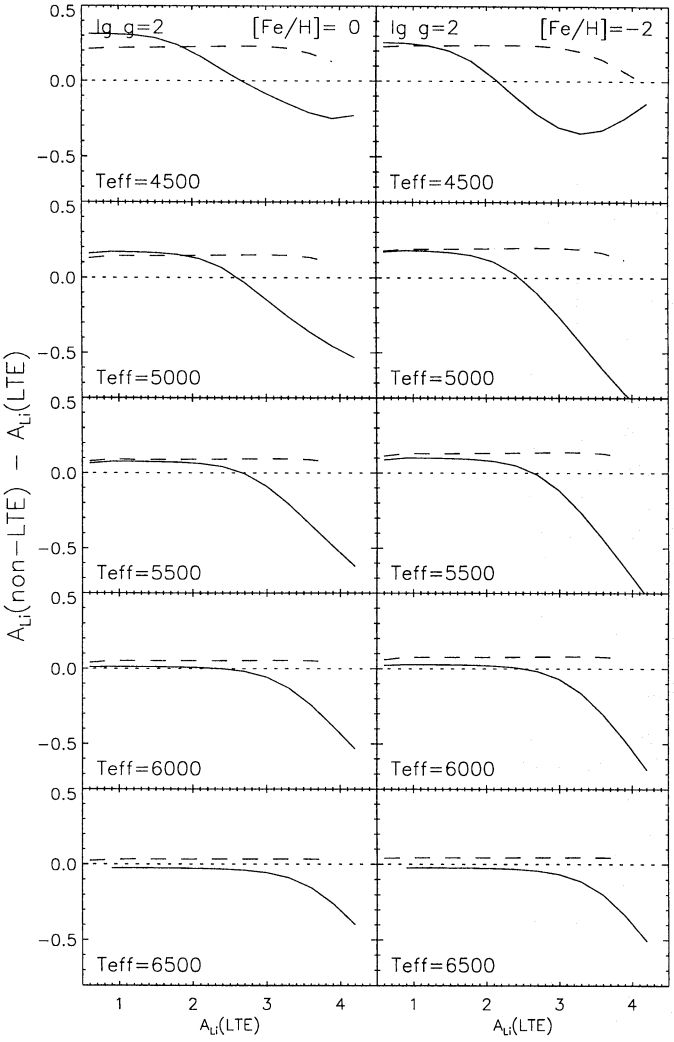

Fig. 17. LTE to non-LTE lithium abundance corrections for subgiants (lg g = 2). Figure coding as in Figs. 10 and 16

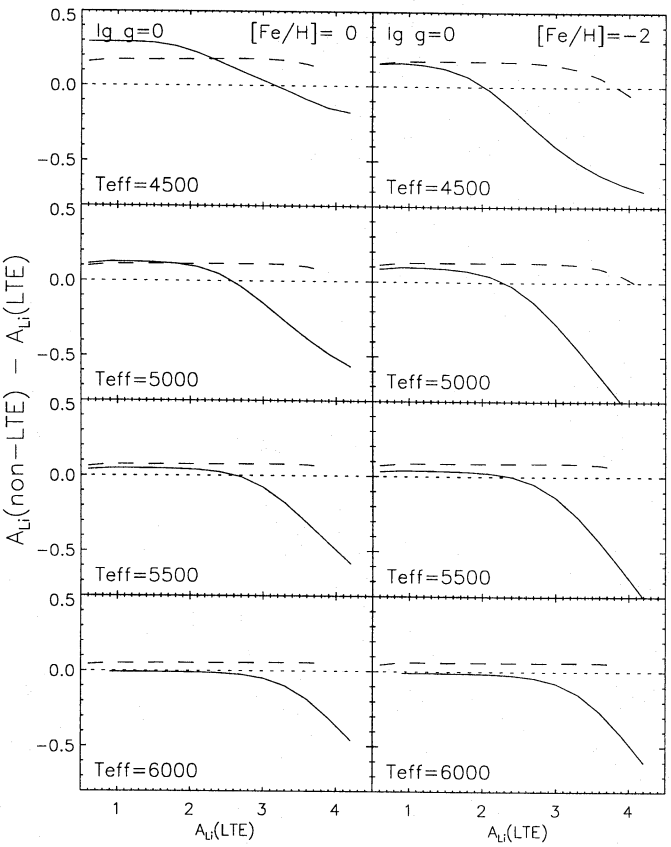

Fig. 18. LTE to non-LTE lithium abundance corrections for giants (lg g = 0). Figure coding as in Figs. 10 and 16

of Fig. 15. The corresponding squares in Fig. 12 are at about the same intensity value; the main difference is a drop in continuum intensity (dash at top right in each panel). However, the LTE height of formation difference is appreciable between left and righthand panels, and so is the difference in non-LTE source function departure. If the line opacity correction didn't reverse, the line would be much weaker; likewise, the larger non-LTE source function correction at right due to the substantial electron density decrease compensates for the flatter temperature gradient of the metal-poor atmosphere. Thus, the emergent profiles are only similar because both non-LTE corrections change appreciably with metallicity.

The LTE to non-LTE differences in the computed flux profiles are quantified in Figs. 16–18 for both Li I 670.8 nm and Li I 610.4 nm. These figures display corrections to LTE abundance analysis in the same manner as in Fig. 10, i.e., in the form of non-LTE corrections that must be applied to the values $A_{\rm Li}^{\rm LTE}$ which result from LTE abundance analysis of our computed profiles. Because these graphs contain the basic results of this paper, we display panels for all values of $T_{\rm eff}$ that we have model atmospheres for, rather than only for the limited selections of Figs. 1–2 and Figs. 11–15. (The results are also given in numerical form in the next section.) The three figures show non-LTE corrections for dwarfs, subgiants and giants, respectively.

The patterns in Figs. 16–18 are qualitatively similar to the young-sun results in Fig. 10; the latter belong between the left-hand $T_{\rm eff}$ = 5500 and $T_{\rm eff}$ = 6000 panels of Fig. 16. Generally, the 670.8 nm curves drop substantially with increasing abundance towards sizable reductions, down to factors of order six (−0.8 dex), while the 610.4 nm curves specify smaller corrections that are positive, and remain more or less flat with increasing abundance. At low abundance, the two curves converge. Roughly, the drops are due to photon losses in the resonance line; the positive corrections to overionization.

In each figure, both corrections decrease with increasing effective temperature from top to bottom. For both the ionization correction and the photon-loss correction, this reduction reflects the diminishing strength of the lithium lines due the to Saha-Boltzmann decrease of the population of the Li I neutral stage that is exhibited in Fig. 12 as general rightward shift of the $A_{\rm Li}$ = 3.3 asterisks with increasing $T_{\rm eff}$.

The same shift in line strength along columns governs the value of the lithium abundance at which the non-LTE influence of resonance-line photon losses becomes noticeable. In the up-

per panels of Fig. 16 this is already the case for $A_{\rm Li}^{\rm LTE} < 2$, in the bottom panels only for $A_{\rm Li}^{\rm LTE} > 3$.

The two corrections compete. For example, the dip in the 670.8 nm curve in the top-left panel of Fig. 16 around $A_{\rm Li}^{\rm LTE} = 3$ is raised by the overionization to corrections near zero rather than $A_{\rm Li} - A_{\rm Li}^{\rm LTE} \approx -0.4$. The upturns of the 670.8 nm curves in the upper panels are due to the convergence of S_l and B_ν seen in Fig. 12. They reflect the difference in the sensitivity of the model temperature to line blanketing and of the 670.8 nm line source function to the radiation field J_l within the line. The 610.4 nm curves have downturns for large $A_{\rm Li}^{\rm LTE}$ that correspond to the small split between the β_{2p} and β_{3d} curves in Fig. 11. The split increases with larger 610.4 nm line strength and so compensates for the effect of the overionization on the line opacity.

The differences in abundance correction due to difference in metallicity are seen when comparing corresponding lefthand and righthand panels in Figs. 16–18. They are small for large $T_{\rm eff}$. For cooler stars, decrease in metallicity does not cause larger corrections for overionization, as one would expect from the corresponding decline of ultraviolet line blocking. Actually, the ionization corrections are slightly larger in the lefthand $T_{\rm eff} = 4500$ panels of Fig. 16 than the righthand ones. This is due to the differences in atmospheric stratification displayed in Figs. 1 and 2. For example, the shallower temperature gradient in the deepest layers of the metal-poor $T_{\rm eff} = 4500$, $\lg g = 4$ atmosphere causes reduction of the $J_c - B_\nu$ excess in the near ultraviolet.

In cool giants (upper panels in Fig. 18) the large reduction in electron density at given optical depth (Fig. 2) causes large difference between the metal-rich case at left and the metal-poor case at right for the 670.8 nm resonance line (solid curves). At left, the source function and opacity corrections cancel each other near $A_{\rm Li}^{\rm LTE} = 3.3$, so that the composite non-LTE correction is zero. At right, the total correction reaches a value of -0.5 dex (reduction to a third) at the same LTE abundance value. The difference corresponds to the difference in vertical separation between the asterisks and squares in the corresponding panels of Fig. 12.

4.5. Numerical recipe

The non-LTE corrections for the Li I 670.8 nm line displayed in Figs. 16–18 are also given in numerical form in Table 1. It specifies a fourth-order polynomial fit in the LTE value $A_{\rm Li}^{\rm LTE}$ to the abundance corrections for all models of our grid. The last column specifies the maximum departure of the fit to the actual results.

These values may be employed to improve LTE abundance determinations from the Li I resonance line. Since the corrections for the 610.4 nm are smaller and possess much less variation across the grid, we refrain from detailing these in a table. Table 1 and appropriate interpolation routines are available through anonymous ftp from ftp.astro.uio.no, directory pub/lithium.

5. Discussion

It is obvious that our results are model dependent. The worst limitation is probably that we have chosen to model lithium line formation for standard flux-constant plane-parallel atmospheres. These are probably not fit to model lithium lines from stars that are both lithium-rich and have very active chromospheres, or from stars with extended envelopes or accretion disks.

Within the constraints of our modeling choices, there are uncertainties due to the model atom and due to the atmosphere modeling. We are confident that are our model atom is sufficiently large and realistic that we have identified the major non-LTE imbalances properly. The major uncertainties come, as usual, from uncertain transition probabilities and cross-sections. Of these, the oscillator strengths for the 670.8 nm resonance line and the 610.4 nm subordinate line and the cross-sections for photoionization from $2s$ and $2p$ are the most important. There is excellent agreement between different sets of theoretical results based on independent methods and between independent theoretical and experimental results; the precision is estimated to be better than 5% (Peach et al. 1988). This uncertainty in the atomic data translates to an uncertainty in the derived non-LTE corrections of less than 0.01 dex.

A major uncertainty in any cool-star modeling of minority ionization stages such as neutral alkalis is the influence of ultraviolet radiation fields, for whose evaluation the line crowding in the near ultraviolet must be taken into account in detail. In order to test the robustness of our choice to employ the opacity distribution function (ODF) formalism of the MARCS code, we have repeated our modeling for dwarfs with $T_{\rm eff} > 4500$ K using opacity sampling (OS). This technique was also employed in the construction of the T5780 model for the sun by Edvardsson et al. (1993), which we have used for the young-sun modeling in Sects. 4.1 and 4.2. The stellar OS results are superimposed on the ODF results in Fig. 16 in the form of dot-dashed curves. For the 610.4 nm line, which senses the ultraviolet radiation fields through the dependency of the $2p$ and $3d$ populations to the ionization balance, the differences are so small that they are nearly invisible. The ODF–OS differences are larger for the 670.8 nm line, especially at lower right, but well within the 0.1 dex noise level which characterizes abundance determination in general.

The ODF–OS differences result primarily from changes of the temperature gradient in the upper photosphere, which directly affects LTE abundance determination because the LTE line strength increases with the gradient. However, a steeper gradient also leads to larger non-LTE overionization which works the other way by weakening the line. The non-LTE corrections cancel the LTE sensitivity to the ODF–OS differences almost entirely, so that the ODF and OS non-LTE curves of growth are very similar. Thus, the dependence of our results on the treatment of the ultraviolet line haze is in fact less than it would have been for LTE analysis.

Figures 16–18 show that the non-LTE corrections to LTE lithium abundance determination utilizing the 670.8 nm resonance line take the form of appreciable reductions for cool stars that are lithium rich, and increases for cool stars that are lithium

Table 1. Numerical approximations to lithium abundance corrections for the 670.8 nm resonance line, given by $\Delta x = a_0+a_1x+a_2x^2+a_3x^3+a_4x^4$ where $x = A_{12}^{\rm LTE}$ and $\Delta x = A_{12} - A_{12}^{\rm LTE}$

lg g	$T_{\rm eff}$	[Fe/H]	a_0	a_1	a_2	a_3	a_4	maximum difference
0.0	4500	0	2.48e-01	8.01e-02	-7.95e-04	-3.22e-02	5.27e-03	0.008
		-1	2.11e-02	4.24e-01	-2.66e-01	3.24e-02	1.54e-04	0.015
		-2	7.25e-03	3.17e-01	-1.41e-01	-2.52e-02	7.48e-03	0.014
	5000	0	2.39e-01	-4.07e-01	4.39e-01	-1.73e-01	1.91e-02	0.012
		-1	2.22e-01	-4.50e-01	4.81e-01	-1.90e-01	2.09e-02	0.012
		-2	2.23e-01	-4.38e-01	4.65e-01	-1.81e-01	1.88e-02	0.012
		-3	2.27e-01	-4.43e-01	4.70e-01	-1.83e-01	1.88e-02	0.012
	5500	0	1.72e-01	-3.69e-01	3.29e-01	-1.05e-01	8.79e-03	0.013
		-1	1.81e-01	-4.29e-01	3.81e-01	-1.22e-01	1.04e-02	0.013
		-2	1.84e-01	-4.22e-01	3.74e-01	-1.19e-01	9.63e-03	0.013
		-3	1.87e-01	-4.27e-01	3.79e-01	-1.21e-01	9.69e-03	0.013
	6000	0	6.78e-02	-1.35e-01	6.42e-02	-1.23e-03	-3.24e-03	0.011
		-1	1.21e-01	-2.49e-01	1.50e-01	-2.64e-02	-9.72e-04	0.012
		-2	1.19e-01	-2.55e-01	1.51e-01	-2.52e-02	-1.48e-03	0.012
		-3	1.29e-01	-2.68e-01	1.61e-01	-2.77e-02	-1.31e-03	0.012
2.0	4500	0	2.21e-01	2.06e-01	-8.94e-02	-2.43e-02	6.61e-03	0.010
		-1	1.11e-01	3.86e-01	-2.33e-01	6.83e-03	5.28e-03	0.015
		-2	7.96e-03	6.11e-01	-3.92e-01	3.93e-02	4.17e-03	0.026
	5000	0	2.52e-01	-3.25e-01	3.81e-01	-1.61e-01	1.87e-02	0.010
		-1	2.82e-01	-4.50e-01	5.08e-01	-2.12e-01	2.48e-02	0.010
		-2	3.31e-01	-5.15e-01	5.54e-01	-2.24e-01	2.49e-02	0.011
		-3	3.36e-01	-5.31e-01	5.70e-01	-2.30e-01	2.54e-02	0.011
	5500	0	2.20e-01	-4.42e-01	4.11e-01	-1.38e-01	1.29e-02	0.015
		-1	2.35e-01	-4.63e-01	4.33e-01	-1.46e-01	1.34e-02	0.015
		-2	2.50e-01	-4.62e-01	4.31e-01	-1.45e-01	1.28e-02	0.016
		-3	2.60e-01	-4.71e-01	4.40e-01	-1.48e-01	1.31e-02	0.016
	6000	0	7.14e-02	-1.55e-01	1.14e-01	-2.44e-02	-5.49e-04	0.014
		-1	9.08e-02	-1.68e-01	1.31e-01	-3.01e-02	-2.21e-04	0.014
		-2	9.42e-02	-1.84e-01	1.41e-01	-3.18e-02	-4.31e-04	0.013
		-3	1.02e-01	-1.89e-01	1.47e-01	-3.42e-02	-2.05e-04	0.014
	6500	0	-6.69e-02	1.20e-01	-1.24e-01	5.38e-02	-8.47e-03	0.005
		-1	-3.38e-02	7.85e-02	-9.65e-02	4.75e-02	-8.22e-03	0.007
		-2	-4.02e-02	7.01e-02	-9.28e-02	4.78e-02	-8.59e-03	0.009
		-3	-2.38e-02	5.77e-02	-8.46e-02	4.59e-02	-8.47e-03	0.009
4.0	4500	0	-6.01e-02	9.51e-01	-7.47e-01	1.87e-01	-1.48e-02	0.024
		-1	-2.34e-01	1.38e+00	-1.14e+00	3.21e-01	-2.94e-02	0.033
		-2	-3.37e-01	1.42e+00	-1.16e+00	3.24e-01	-2.97e-02	0.034
	5000	0	3.12e-01	-5.14e-01	5.75e-01	-2.42e-01	3.00e-02	0.011
		-1	2.88e-01	-5.09e-01	6.00e-01	-2.65e-01	3.42e-02	0.019
		-2	2.22e-01	-3.76e-01	4.87e-01	-2.27e-01	3.01e-02	0.029
		-3	1.95e-01	-4.37e-01	5.23e-01	-2.31e-01	2.98e-02	0.026
	5500	0	2.46e-01	-5.46e-01	5.12e-01	-1.78e-01	1.81e-02	0.016
		-1	2.95e-01	-6.66e-01	6.27e-01	-2.21e-01	2.30e-02	0.019
		-2	3.10e-01	-7.27e-01	6.82e-01	-2.41e-01	2.54e-02	0.020
		-3	3.22e-01	-7.46e-01	7.02e-01	-2.49e-01	2.65e-02	0.020
	6000	0	9.75e-02	-2.51e-01	1.99e-01	-5.43e-02	2.89e-03	0.014
		-1	1.20e-01	-2.82e-01	2.31e-01	-6.52e-02	3.84e-03	0.015
		-2	1.28e-01	-3.17e-01	2.60e-01	-7.42e-02	4.62e-03	0.015
		-3	1.37e-01	-3.21e-01	2.67e-01	-7.77e-02	5.07e-03	0.015
	6500	0	-3.03e-02	2.02e-03	-3.04e-02	2.45e-02	-5.52e-03	0.009
		-1	-3.43e-03	-3.76e-02	-5.31e-03	1.91e-02	-5.39e-03	0.010
		-2	8.66e-03	-7.23e-02	1.82e-02	1.32e-02	-5.05e-03	0.010
		-3	3.00e-02	-9.16e-02	3.24e-02	9.04e-03	-4.65e-03	0.011
	7000	0	-1.75e-01	2.71e-01	-2.22e-01	7.81e-02	-1.02e-02	0.001
		-1	-2.01e-01	3.07e-01	-2.51e-01	8.84e-02	-1.16e-02	0.001
		-2	-1.93e-01	2.93e-01	-2.43e-01	8.71e-02	-1.17e-02	0.002
		-3	-1.70e-01	2.80e-01	-2.36e-01	8.56e-02	-1.16e-02	0.002

Table 1. (continued)

lg g	$T_{\rm eff}$	[Fe/H]	a_0	a_1	a_2	a_3	a_4	maximum difference
4.0	7500	0	-1.60e-01	2.18e-01	-1.77e-01	6.07e-02	-7.52e-03	0.002
		-1	-2.29e-01	3.11e-01	-2.42e-01	7.99e-02	-9.69e-03	0.002
		-2	-2.30e-01	3.27e-01	-2.55e-01	8.47e-02	-1.03e-02	0.002
		-3	-2.30e-01	3.47e-01	-2.64e-01	8.60e-02	-1.03e-02	0.002
4.5	4500	0	-4.72e-02	9.17e-01	-7.43e-01	1.93e-01	-1.59e-02	0.023
		-1	-2.14e-01	1.30e+00	-1.10e+00	3.20e-01	-3.07e-02	0.029
		-2	-3.31e-01	1.14e+00	-9.02e-01	2.44e-01	-2.17e-02	0.028
	5000	0	2.65e-01	-4.10e-01	4.96e-01	-2.22e-01	2.87e-02	0.019
		-1	1.65e-01	-1.97e-01	3.30e-01	-1.76e-01	2.47e-02	0.034
		-2	1.01e-01	-1.25e-01	2.53e-01	-1.42e-01	2.02e-02	0.032
		-3	1.15e-01	-3.69e-01	4.18e-01	-1.81e-01	2.30e-02	0.023
	5500	0	2.67e-01	-6.18e-01	5.81e-01	-2.04e-01	2.15e-02	0.017
		-1	3.17e-01	-7.53e-01	7.11e-01	-2.54e-01	2.76e-02	0.020
		-2	3.12e-01	-7.79e-01	7.32e-01	-2.61e-01	2.86e-02	0.020
		-3	3.13e-01	-7.75e-01	7.28e-01	-2.60e-01	2.85e-02	0.020
	6000	0	2.71e-01	-5.95e-01	4.29e-01	-1.19e-01	9.29e-03	0.012
		-1	1.34e-01	-3.40e-01	2.83e-01	-8.44e-02	6.30e-03	0.016
		-2	1.45e-01	-3.82e-01	3.18e-01	-9.57e-02	7.42e-03	0.016
		-3	1.56e-01	-3.91e-01	3.30e-01	-1.00e-01	8.04e-03	0.017
	6500	0	-2.15e-02	-2.55e-02	-7.66e-03	1.69e-02	-4.64e-03	0.009
		-1	4.19e-03	-7.36e-02	2.40e-02	9.34e-03	-4.27e-03	0.010
		-2	1.14e-02	-9.87e-02	4.34e-02	3.83e-03	-3.88e-03	0.011
		-3	3.86e-02	-1.28e-01	6.39e-02	-1.98e-03	-3.31e-03	0.011
	7000	0	-1.69e-01	2.50e-01	-2.06e-01	7.32e-02	-9.68e-03	0.001
		-1	-2.15e-01	3.13e-01	-2.50e-01	8.69e-02	-1.14e-02	0.002
		-2	-1.89e-01	2.75e-01	-2.27e-01	8.21e-02	-1.11e-02	0.003
		-3	-1.65e-01	2.57e-01	-2.16e-01	7.92e-02	-1.09e-02	0.003
	7500	0	-1.85e-01	2.58e-01	-2.01e-01	6.68e-02	-8.13e-03	0.002
		-1	-2.67e-01	3.73e-01	-2.79e-01	8.98e-02	-1.07e-02	0.002
		-2	-2.74e-01	4.00e-01	-2.99e-01	9.61e-02	-1.14e-02	0.002
		-3	-2.19e-01	3.27e-01	-2.52e-01	8.34e-02	-1.02e-02	0.001

poor. The corrections increase when the metallicity decreases, and differ also with gravity for the coolest stars. These trends imply that making comparisons of LTE-derived abundances between different stars to test evolution scenarios runs the risk of wrongly interpreting gradients or parts of gradients that are actually caused by non-LTE line formation. We test such sensitivity here by showing adjustments to two gradients displayed in the literature.

Figure 19 is a non-LTE update of a plot in Boesgaard (1990a), also published in Boesgaard (1991). It shows mean lithium abundances for stars with $5950 < T_{\rm eff} < 6400$ K in eight clusters as a function of cluster age. The upper panel is equivalent with but not identical to Boesgaard's plot. We have used a similar data compilation, taken from the sources listed by Boesgaard (1991), but we have increased the upper limit of the temperature range from 6350 K to 6400 K. The differences in adopted LTE abundances and data selection criteria lower the value for α Per (leftmost data point) and raises the halo star mean (asterisk at right) from $A_{\rm Li}^{\rm LTE} = 2.1$ to 2.2. The dotted line specifies Boesgaard's original fit to the four solar-metallicity clusters, the solid line is ours. It is slightly lower but it has the same slope. The difference shows the sensitivity of the fit to data selection criteria.

The lower panel is a similar plot, obtained after we applied non-LTE corrections according to our results above to each star before taking the cluster averages. The dotted line is again Boesgaard's fit. The non-LTE fit (solid) has a different slope, flattened from $A_{\rm Li}^{\rm LTE} \sim -0.29\,\lg$ (age in years) to $A_{\rm Li} \sim -0.25\,\lg$ (age in years). The slope diminishes because the lithium-rich stars at left require substantial downward corrections; yet larger corrections apply to the Hyades stars (square). The scatter is also smaller, again especially for the Hyades. These differences are significant, demonstrating that interpretations of such measurements need to take non-LTE effects into account. For example, Boesgaard (1990, 1991) used the high value of the Hyades in the upper panel to vindicate the hypothesis of microscopic diffusion; this may be premature.

Figure 20 is a similar re-issue of published material, in this case emulating Fig. 4 of Rebolo et al. (1988) from a data compilation based on the sources they list. Both the non-LTE and the LTE result of fitting the observed 670.8 nm line strength are plotted for stars with extreme metal deficiency (pluses) and for Hyades members (dots); the larger symbols represent the non-LTE results. The non-LTE corrections (vertical shifts from the smaller to the larger symbols) are downward at left and upward at right (cf. Fig. 16). As a result, the non-LTE fit for the very

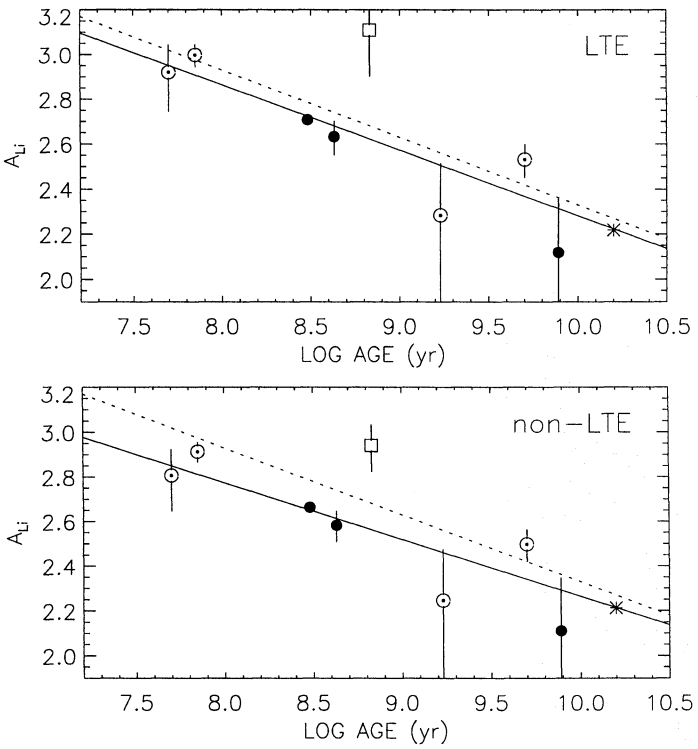

Fig. 19. Mean lithium abundance determined from the 670.8 nm line in eight clusters, plotted against cluster age after Boesgaard (1991). Upper panel: LTE abundances; lower panel: non-LTE abundances. Solid: linear fit to four clusters with solar metallicity. Dashed: Boesgaard's original relation for the same clusters, shown in both panels for reference. The clusters are, from left to right: α Per, Pleiades, UMa, Coma, Hyades, NGC 752, M 67 and NGC 188. The symbol coding is the same as in Boesgaard (1991): $\odot$ designates the clusters with solar metallicity, the square is for the higher-metallicity Hyades, filled circles are clusters of lower metallicity, the asterisk at right represents halo dwarfs. The error bars are plus-minus the standard deviation in the mean of the non-logarithmic abundance values per cluster

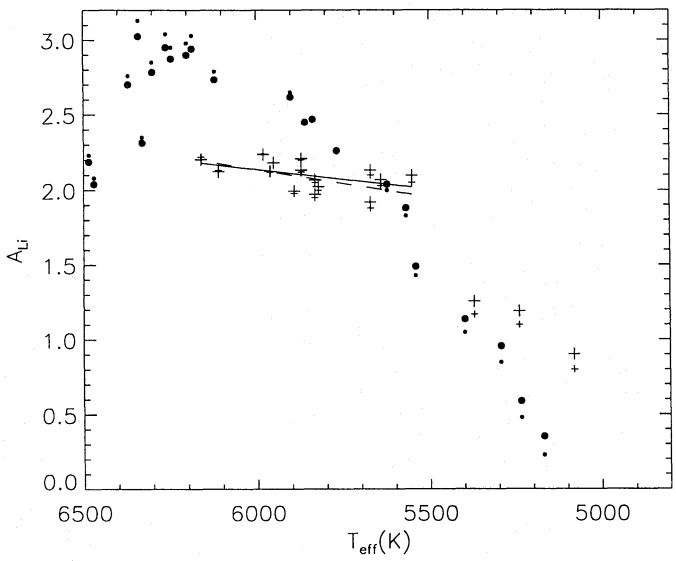

Fig. 20. Lithium abundance determined from the 670.8 nm line plotted against effective temperature, after Fig. 4 of Rebolo et al. (1988). Dots are stars in the Hyades, pluses are stars with extremely low metallicity, [Fe/H] < -1.4. Each star appears twice. The larger symbol marks the non-LTE result, the smaller is for LTE abundance estimation. The two lines are linear fits for the extreme metal-deficient stars, for non-LTE (solid) and LTE (dashed) respectively

metal-deficient stars (pluses) has a flatter gradient then the LTE fit.

6. Conclusions

The many uncertainties that beset stellar abundance determination typically produce a noise level at about 0.1 dex accuracy; non-LTE corrections are important when they exceed this value. The curves in Figs. 16–18 show that this is the case in Li I 670.8 nm abundance determination for all lithium-rich stars, and also for lithium-poor stars that are cool. The latter stars require comparable non-LTE corrections for the weaker 610.4 nm line. In general, in the many debates that continue to be excited by stellar lithium lines, it is necessary that detailed non-LTE abundance analysis rather than the ubiquitous LTE abundance estimation is achieved whenever abundance differences between stars are discussed in the $\Delta A_{\rm Li} = 0.1 - 0.5$ dex regime.

In this paper, we have limited ourselves to a study permitting self-consistency by neglecting chromospheres, disks, spotted surfaces, etc. Within this constraint, the analysis is complete in the sense that all phenomena seen in the line formation diagnostics in Sects. 4.1 and 4.3 tie together in self-consistent manner to produce the results in Sects. 4.2 and 4.4. We have found that:

- the non-LTE mechanisms in lithium line formation across our cool-star grid are straightforward and pose no unexpected surprise;
- the sign and the size of the non-LTE corrections vary across the grid, in fairly intricate manner which is partially controlled by competition between different mechanisms;
- the corrections are largest for lithium-rich cool stars and for lithium-poor cool stars, with opposite sense between these two categories;
- the corrections cause changes in the slope of various observed lithium abundance relationships that play a role in ongoing lithium debates;
- it is useful to include the Li I 610.4 nm line in lithium abundance determinations; at large lithium abundance, its non-LTE corrections are opposite to those of the 670.8 nm resonance line.

The last finding confirms Duncan's (1991) suggestion which triggered our study.

A final warning is that the non-LTE corrections displayed here hold only for the stellar atmosphere models from which they were computed. The various competitions between parameters and mechanisms that are displayed in Sect. 4.3 imply that no general recipes can be formulated from our results. For other atmospheric stratifications, similarly detailed non-LTE analysis is required to evaluate non-LTE departures in lithium lines. For

example, the large spread seen in the Pleiades for stars cooler than $T_{\rm eff} \approx 5500$ K cannot simply be attributed to star-to-star variations in lithium abundance before such evaluation is done. The fact that the K I 769.9 nm resonance line displays qualitatively similar strength variations which similarly correlate with changes in Ca II 854.2 nm and Hα (Figs. 2c and 4 of Soderblom et al. 1993) immediately says that there are substantial variations between Pleiades stars in atmospheric stratification which are not covered by our models.

Acknowledgements. We are indebted to Douglas K. Duncan for suggesting this analysis. M. Carlsson acknowledges support from the Norwegian Research Council (NFR). R.J. Rutten acknowledges the inspiring hospitality of the National Solar Observatory/Sacramento Peak where he held a Fulbright Scholarship granted by the Netherlands-America Commission for Educational Exchange. N.G. Shchukina acknowledges travel support from the Netherlands Organization for Scientific Research (NWO) and hospitality at the Sterrekundig Instituut Utrecht.

References

Abia, C., Boffin, H. M. J., Isern, J., Rebolo, R. 1991, A&A, 245, L1
Ahrens, B., Stix, M., Thorn, M. 1992, A&A, 264, 673
Alcock, C., Fuller, G., Mathews, G. 1987, ApJ, 320, 439
Allen, C. W. 1976, Astrophysical Quantities, Athlone Press, Univ. London
Ambruster, C. W., Fekel, F. C., Guinan, E. F. 1992, in M. S. Giampapa, J. A. Bookbinder (eds.), Seventh Cambridge, Workshop on Cool Stars, Stellar Systems and the Sun, Astron. Soc. Pac. Conf. Series 26, p. 569
Anders, E., Grevesse, N. 1989, Geochim. Cosmochim. Acta, 53, 197
Andretta, V., Gomez, M. T., Severino, G. 1991, Solar Phys., 131, 1
Athay, R. G., Lites, B. W. 1972, ApJ, 176, 809
Audouze, J., Silk, J. 1989, ApJ, 342, L5
Auman, J. R., Woodrow, J. E. J. 1975, ApJ, 197, 163
Balachandran, S. 1991, in F. D'Antona (ed.), The Problem of Lithium, Proc. Workshop Monte Porzio, Mem. Soc. Astron. Ital., Vol. 62, No. 1, p. 33
Balachandran, S., Lambert, D. L., Stauffer, J. R. 1988, ApJ, 333, 267
Barbuy, B., Jorissen, A., Rossi, S. C. F., Arnould, M. 1992, A&A, 262, 216
Bashkin, S., Stoner, J. O. 1975, Atomic Energy Levels and Grotrian Diagrams, North-Holland Publ. Co., Amsterdam
Basri, G., Martin, E. L., Bertout, C. 1991, A&A, 252, 625
Biémont, E., Grevesse, N. 1973, Atomic Data and Nuclear Data Tables, 12, 217
Bodenheimer, P. 1965, ApJ, 142, 451
Boesgaard, A. M. 1988, Proc. 4th Asian–Pacific Reg. Meeting IAU, Vistas Astron., 31, 167
Boesgaard, A. M. 1990a, in K. James (ed.), The formation and evolution of star clusters, Proc. 102nd Summer Meeting ASP, Astron. Soc. Pac. Conf. Series 13, p. 463
Boesgaard, A. M. 1990b, in G. Wallerstein (ed.), Cool Stars, Stellar Systems and the Sun, Proc. Sixth Cambridge Workshop, Astron. Soc. Pac. Conf. Series 9, p. 317
Boesgaard, A. M. 1991, ApJ, 370, L95
Boesgaard, A. M., Steigman, G. 1985, ARA&A, 23, 317
Boesgaard, A. M., Tripicco, M. J. 1986, ApJ, 302, L49
Bonsack, W. K., Greenstein, J. L. 1960, ApJ, 131, 83
Brault, J., Noyes, R. 1983, ApJ, 269, L61
Brown, J. A., Sneden, C., Lambert, D. L., Dutchover, E. 1989, ApJS, 71, 293
Brown, L. E. 1992, ApJ, 389, 251
Brown, L. E., Dearborn, D. S., Schramm, D. N., Larsen, J. T., Kurokawa, S. 1991, ApJ, 371, 648
Bruls, J. H. M. J., Rutten, R. J., Shchukina, N. G. 1992, A&A, 265, 237
Caccin, B., Gomez, M. T., Severino, G. 1993, A&A, 276, 219
Cameron, A. G. W. 1955, ApJ, 121, 144
Cameron, A. G. W., Fowler, W. A. 1971, ApJ, 164, 111
Carlsson, M. 1986, A Computer Program for Solving Multi-Level Non-LTE Radiative Transfer Problems in Moving or Static Atmospheres, Report No. 33, Uppsala Astronomical Observatory
Carlsson, M., Rutten, R. J., Shchukina, N. G. 1992, A&A, 253, 567
Cayrel, R. 1991, Ann. de Physique, 16, 155
Charbonnel, C., Vauclair, S. 1992, A&A, 265, 55
Charbonnel, C., Vauclair, S., Zahn, J.-P. 1992, A&A, 255, 191
Chiemelewski, Y., Friel, E., de Strobel, G. C., Bentolila, C. 1992, A&A, 263, 219
Christensen-Dalsgaard, J., Gough, D. O., Thompson, M. J. 1992, A&A, 264, 518
Cohen, J. G. 1974, PASP, 86, 31
D'Antona, F. (ed.) 1991, The Problem of Lithium, Proc. Workshop Monte Porzio, Mem. Soc. Astr. Ital. 62, No. 1
D'Antona, F., Matteucci, F. 1991, A&A, 248, 62
De la Reza, R., Torres, C. A. O., Busko, I. C. 1981, MNRAS, 194, 829
De Medeiros, J. R., Lèbre, A. 1992, A&A, 264, L21
Dearborn, D. S. P., Schramm, D. N., Hobbs, L. M. 1992, ApJ, 394, L61
Dearborn, D. S. P., Schramm, D. N., Steigman, G., Truran, J. 1989, ApJ, 347, 455
Deliyannis, C. P., Demarque, P. 1991a, ApJ, 379, 216
Deliyannis, C. P., Demarque, P. 1991b, ApJ, 370, L89
Deliyannis, C. P., Pinsonneault, M. H. 1992, in M. S. Giampapa, J. A. Bookbinder (eds.), Seventh Cambridge Workshop on Cool Stars, Stellar Systems and the Sun, Astron. Soc. Pac. Conf. Series 26, p. 573
Denn, G. R., Luck, R. E., Lambert, D. L. 1991, ApJ, 377, 657
Dimitrijević, M. S., Sahal-Bréchot, S. 1991, J. Quant. Spectrosc. Radiat. Transfer, 46, 41
Dravins, D., Linde, P., Ayres, T. R., Linsky, J. L., Monsignori-Fossi, B., Simon, T., Wallinder, F. 1993a, ApJ, 403, 412
Dravins, D., Linde, P., Fredga, K., Gahm, G. F. 1993b, ApJ, 403, 396
Dravins, D., Lindegren, L., Nordlund, Å., VandenBerg, D. A. 1993c, ApJ, 403, 385
Drawin, H.-W. 1968, Zeitschrift f. Physik, 211, 404
Drawin, H. W. 1969, Zeitschrift f. Physik, 225, 483
Duncan, D. K. 1981, ApJ, 248, 651
Duncan, D. K. 1991, ApJ, 373, 250
Duncan, D. K., Jones, B. F. 1983, ApJ, 271, 663
Duncan, D. K., Lambert, D. L., Lemke, M. 1992, ApJ, 401, 584
Edvardsson, B., Andersen, J., Gustafsson, B., Lambert, D. L., Nissen, P. E., Tomkin, J. 1993, A&A, 275, 101
Engvold, O., Kjeldseth Moe, O., Maltby, P. 1970, A&A, 9, 79
Fekel, F. C., Balachandran, S. 1993, ApJ, 403, 708
Fekel, F. C., Marschall, L. A. 1991, AJ, 102, 1439
García López, R. J., Rebolo, R., Herrero, A., Beckman, J. E. 1993, ApJ, 412, 173

García López, R. J., Spruit, H. C. 1991a, in F. D'Antona (ed.), The Problem of Lithium, Proc. Workshop Monte Porzio, Mem. Soc. Astron. Ital., Vol. 62, No. 1, p. 183
García López, R. J., Spruit, H. C. 1991b, A&A, 377, 268
Giampapa, M. S. 1984, ApJ, 277, 235
Gilmore, G., Edvardsson, B., Nissen, P. E. 1991, ApJ, 378, 17
Gilmore, G., Gustafsson, B., Edvardsson, B., Nissen, P. E. 1992, Nat, 357, 379
Greenstein, J. L., Richardson, R. S. 1951, ApJ, 113, 536
Grevesse, N. 1968, Solar Phys., 5, 159
Gustafsson, B. 1973, Uppsala Astr. Obs. Ann., 5, No. 6
Gustafsson, B., Bell, R. A., Eriksson, K., Nordlund, Å.. 1975, A&A, 42, 407
Herbig, G. H. 1965, ApJ, 141, 588
Hobbs, L. M., Pilachowski, C. 1988, ApJ, 334, 734
Hobbs, L. M., Thorburn, J. A. 1991, ApJ, 375, 116
Hofsaess, D. 1979, Atomic Data and Nuclear Data Tables, 24, 285
Hummer, D. G. 1968, MNRAS, 138, 73
Hunger, K. 1957, AJ, 62, 294
Iben, I. V. 1965, ApJ, 142, 1447
Iben, I. V. 1966, ApJ, 143, 483
Iben, I. V. 1967, ApJ, 147, 624
Jin, L. 1990, ApJ, 356, 501
Kaulakys, B. 1985, J. Phys. B: At. Mol. Phys., 18, L167
Kaulakys, B. 1986, Sov. Phys. JETP, 64, 229
Krauss, L. M., Romanelli, P. 1990, ApJ, 358, 47
Kurucz, R. L. 1990, in J. E. Hansen (ed.), Atomic Spectra and Oscillator Strengths for Astrophysics and Fusion Research, North Holland, Amsterdam, p. 20
Kurucz, R. L. 1991, in L. Crivellari, I. Hubeny,, D. G. Hummer (eds.), Stellar Atmospheres: Beyond Classical Models, NATO ASI Series C-341, KLuwer, Dordrecht, p. 441
Lambert, D. L., Heath, J. E., Edvardsson, B. 1991, MNRAS, 253, 610
Lambert, D. L., Smith, V. V., Heath, J. 1993, PASP, 105, 568
Lemke, M., Lambert, D. L., Edvardsson, B. 1993, PASP, 105, 468
Lemoine, M., Ferlet, R., Vidal-Madjar, A., Emerich, C., Bertin, P. 1993, A&A, 269, 469
Lites, B. W. 1972, Observation and Analysis of the Solar Neutral Iron Spectrum, NCAR Cooperative Thesis No. 28, High Altitude Observatory, Boulder
Luck, R. E. 1977, ApJ, 218, 752
Magazzu, A., Martin, E. L., Rebolo, R. 1991, A&A, 249, 149
Magazzù, A., Rebolo, R., Pavlenko, Y. V. 1992, ApJ, 392, 159
Malaney, R. A. 1992, ApJ, 398, L45
Malaney, R. A., Fowler, W. A. 1988, ApJ, 333, 14
Martin, E. L., Magazzu, A., Rebolo, R. 1992a, A&A, 257, 186
Martin, E. L., Rebolo, R., Casares, J., Charles, P. A. 1992b, Nat, 358, 129
Mathews, G. J., Alcock, C. R., Fuller, G. M. 1990, ApJ, 349, 449
Mathisen, R. 1984, Oslo Inst. Theor. Astrophys. Publ. Series, 1, 1
McKellar, A. 1940, PASP, 52, 407
Meneguzzi, M., Audouze, J., Reeves, H. 1971, A&A, 15, 337
Meneguzzi, M., Reeves, H. 1975, A&A, 40, 99
Menzel, D. H., Cillié, G. G. 1937, ApJ, 85, 88
Michaud, G., Charbonneau, P. 1991, Space Sc. Rev., 57, 2
Michaud, G., Fontaine, G., Beaudet, G. 1984, ApJ, 282, 206
Michaud, G., Richer, J. 1991, in F. D'Antona (ed.), The Problem of Lithium, Proc. Workshop Monte Porzio, Mem. Soc. Astron. Ital., Vol. 62, No. 1, p. 151
Mihalas, D. 1978, Stellar Atmospheres, W. H. Freeman and Co., San Francisco (second edition)
Molaro, P. 1991, in F. D'Antona (ed.), The Problem of Lithium, Proc. Workshop Monte Porzio, Mem. Soc. Astron. Ital., Vol. 62, No. 1, p. 17
Müller, E. A., Peytremann, E., De la Reza, R. 1975, Solar Phys., 41, 53
Murphy, R. J., Hua, X.-M., Kozlovsky, B., Ramaty, R. 1990, ApJ, 351, 299
Olive, K. A., Schramm, D. N. 1992, Nat, 360, 439
Olson, G. L., Auer, L. H., Buchler, J. R. 1986, J. Quant. Spectrosc. Radiat. Transfer, 35, 431
Padgett, D. L. 1990, in G. Wallerstein (ed.), Cool Stars, Stellar Systems and the Sun, Proc. Sixth Cambridge Workshop, Astron. Soc. Pac. Conf. Series 9, p. 354
Pallavicini, R., Cutisposo, G., Randich, S., Gratton, R. 1993, A&A, 267, 145
Pallavicini, R., Randich, S., Giampapa, M. S. 1992, A&A, 253, 185
Park, C. 1971, J. Quant. Spectrosc. Radiat. Transfer, 11, 7
Pavlenko, Y. V. 1989, Kinematika i Fizika Nebesnykh Tel., 5, 55
Pavlenko, Y. V. 1990, Kinematika i Fizika Nebesnykh Tel., 6, 58
Pavlenko, Y. V. 1991a, SvA, 35, 384
Pavlenko, Y. V. 1991b, SvA, 35, 623
Peach, G., Saraph, H., Seaton, M. 1988, J. Phys. B, 21, 3669
Peebles, P. J. E. 1966, Phys. Rev. Lett., 16, 410
Pilachowski, C. A., Sneden, C., Booth, J. 1993, ApJ, 407, 699
Pilachowski, C. A., Sowell, J. R. 1992, AJ, 103, 1668
Pinsonneault, M. H., Deliyannis, C. P., Demarque, P. 1992, ApJS, 78, 179
Pinsonneault, M. H., Kawaler, S. D., Demarque, P. 1990, ApJS, 74, 501
Pinsonneault, M. H., Kawaler, S. D., Sofia, S., Demarque, P. 1989, ApJ, 338, 424
Proffit, C. R., Michaud, G. 1989, ApJ, 346, 976
Puls, J., Herrero, A. 1988, A&A, 204, 219
Randich, S., Gratton, R., Pallavicini, R. 1993, A&A, 273, 194
Randich, S., Mark S, G., Pallavicini, R. 1992, in M. S. Giampapa, J. A. Bookbinder (eds.), Seventh Cambridge Workshop on Cool Stars, Stellar Systems and the Sun, Astron. Soc. Pac. Conf. Series, Vol. 26, p. 576
Rebolo, R. 1990, in F. Sanchez, M. Vazquez (eds.), New Windows to the Universe, Proc. XI ERAM IAU, Cambrige Univ. Press, Cambridge
Rebolo, R. 1991, in G. Michaud, A. Tutukov (eds.), The Photospheric Abundance Connection, Proc. IAU Symp. 145, Kluwer, Dordrecht, p. 85
Rebolo, R., Martin, E. L., Magazzu, A. 1992, ApJ, 389, L83
Rebolo, R., Molaro, P., Beckman, J. E. 1988, A&A, 192, 192
Reeves, H. 1993, A&A, 269, 166
Reeves, H., Fowler, W. A., Hoyle, F. 1970, Nat, 226, 727
Reeves, H., Richter, J., Sato, K., Terasawa, N. 1990, ApJ, 355, 18
Rutten, R. J. 1988, in R. Viotti, A. Vittone,, M. Friedjung (eds.), Physics of Formation of FeII Lines Outside LTE, IAU Colloquium 94, Reidel, Dordrecht, p. 185
Rutten, R. J. 1990, in G. Wallerstein (ed.), Cool Stars, Stellar Systems and the Sun, Proc. Sixth Cambridge Workshop, Astron. Soc. Pac. Conf. Series 9, p. 91
Rutten, R. J., Carlsson, M. 1994, in D. M. Rabin, J. T. Jefferies,, C. Lindsey (eds.), Infrared Solar Physics, Proc. Symp. 154 IAU (Tucson), Kluwer, Dordrecht, p. 309
Sackmann, I.-J., Boothroyd, A. I. 1992, ApJ, 392, L71
Scalo, J. M. 1976, ApJ, 206, 795
Scalo, J. M., Ulrich, R. K. 1973, ApJ, 183, 151
Scharmer, G. B., Carlsson, M. 1985, J. Comput. Phys., 59, 56

Schatzman, E. 1991, in F. D'Antona (ed.), The Problem of Lithium, Proc. Workshop Monte Porzio, Mem. Soc. Astron. Ital., Vol. 62, No. 1, p. 111
Schatzman, E., Baglin, A. 1991, A&A, 249, 125
Schwarzschild, M. 1957, Structure and evolution of the stars, Dover Publ., New York
Smith, V. V., Lambert, D. L. 1986, ApJ, 303, 226
Smith, V. V., Lambert, D. L. 1989, ApJ, 345, L75
Smith, V. V., Lambert, D. L. 1990, ApJ, 361, L69
Smith, V. V., Lambert, D. L., Nissen, P. E. 1993, ApJ, 408, 262
Soderblom, D. R. 1991, in F. D'Antona (ed.), The Problem of Lithium, Proc. Workshop Monte Porzio, Mem. Soc. Astron. Ital., Vol. 62, No. 1, p. 43
Soderblom, D. R., Jones, B. F., Balachandran, S., Stauffer, J. R., Duncan, D. K., Fedele, S. B., Hudon, J. D. 1993a, AJ, 106, 1059
Soderblom, D. R., Oey, M. S., Johnson, D. R. H., Stone, R. P. S. 1990, AJ, 99, 595
Soderblom, D. R., Pilachowski, C. A., Fedele, S. B., Jones, B. F. 1993b, AJ, 105, 2299
Soderblom, D. R., Stauffer, J. R., MacGregor, K. B., Jones, B. F. 1993c, ApJ, 409, 624
Spite, F. 1990, in R. Pallavicini (ed.), High Resolution Spectroscopy in Astrophysics, Mem. Soc. Astron. Ital., Vol. 61, No. 3, p. 663
Spite, F. 1991, in F. D'Antona (ed.), The Problem of Lithium, Proc. Workshop Monte Porzio, Mem. Soc. Astron. Ital., Vol. 62, No. 1, p. 11
Spite, F., Spite, M. 1982, A&A, 115, 357
Spite, F., Spite, M. 1986, A&A, 163, 140
Spite, F., Spite, M. 1993, A&A, 279, L9
Spite, M., Maillard, J. P., Spite, F. 1984, A&A, 141, 56
Spite, M., Molaro, P., Francois, P., Spite, F. 1993, A&A, 271, L1
Spitzer, L. 1949, ApJ, 109, 549
Stauffer, J. R., Prosser, C. F., Giampapa, M. S., Soderblom, D. R., Simon, T. 1993, AJ, 106, 229
Steenbock, W., Holweger, H. 1984, A&A, 130, 319
Steigman, G. 1993, Phys. Reports, 227, 243
Steigman, G., Walker, T. P. 1992, ApJ, 385, L13
Strom, K. M., Wilkin, F. P., Strom, S. E. 1989, AJ, 98, 1444
Swenson, F. J., Faulkner, J. 1992, ApJ, 395, 654
Thorburn, J. A. 1992, ApJ, 399, L83
Thorburn, J. A., Beers, T. C. 1993, ApJ, 404, L13
Thorburn, J. A., Hobbs, L. M., Deliyannis, C. P., Pinsonneault, M. H. 1993, ApJ, 415, 150
Truran, J. W., Cameron, A. G. W. 1971, Astrophys. Space Sci., 14, 179
Unsöld, A. 1955, Physik der Sternatmosphären, Springer Verlag, Berlin (second edition)
Vauclair, S. 1988, ApJ, 335, 971
Wagoner, R. V. 1973, ApJ, 179, 343
Wagoner, R. V., Fowler, W. A., Hoyle, F. 1967, ApJ, 148, 3
Walker, T. P., Steigman, G., Schramm, D. N., Olive, K. A., Kang, H.-S. 1991, ApJ, 376, 51
Wallerstein, G. 1992, Nat, 356, 569
Wallerstein, G., Herbig, G. H., Conti, P. S. 1965, ApJ, 141, 610
Wiese, W. L., Smith, M. W., Glennon, B. M. 1966, Atomic Transition Probabilities Volume I. Hydrogen through Neon, NSRDS-NBS Ref. Data Ser. 4, Natl. Bur. Standards, Washington
Wijbenga, J. W., Zwaan, C. 1972, Solar Phys., 23, 265
Xue-Fu, L., Gang, Z., Hui-Song, T., Fang-Jun, L. 1992, Acta Astron. Sinica, 33, 316
Yang, J., Turner, M. S., Steigman, G., Schramm, D. N., Olive, K. A. 1984, ApJ, 281, 493
Zahn, J.-P. 1992, A&A, 265, 115

This article was processed by the author using Springer-Verlag LaTeX A&A style file version 3.